Master of Science

# Properties of g-$C_3N_4$/ZnO composite photocatalyst : Annealing temperature and Precursor effect

The Graduate School of the University of Ulsan

Department of Chemical Engineering

Haewon Jung

# *Properties of g-$C_3N_4$/ZnO composite photocatalyst : Annealing temperature and Precursor effect*

Supervisor: Professor Eun Woo Shin

A Dissertation

Submitted to

The Graduate School of the University of Ulsan

In partial Fulfillment of the Requirements

for the Degree of

Master of Science

by

Haewon Jung

School of Chemical Engineering

Ulsan, South Korea

February 2019

***Properties of g-$C_3N_4$/ZnO composite photocatalyst :***

***Annealing temperature and Precursor effect***

This certifies that the master's thesis

of Haewon Jung is approved.

---

Committee Chair Prof. Won mook Choi

---

Committee Member Prof. Eun Woo Shin

---

Committee Member Prof. Sunwook Kim

Department of Chemical Engineering

Ulsan, South Korea

February 2019

## Acknowledgement

Firstly, I would like to sincerely express my gratitude my supervisor, Professor Eun Woo Shin for giving me an excellent guidance, expert advice through every moments of my master course. I have learned the means of research as well as a lot of attitude for life from him. I would like to thank all of the members of my committee, Professor Sunwook Kim and Professor Wonmook Choi for their advice and contributions to this work.

Thanks to all lab members, Thanh-Truc Pham, Nguyen Phu Huy, Do Thi Lien, Nguyen Kim Ahn, Hong An Yu, Mingyan Wang and Kaiming Jiang for their professional supports in researching and their friendships. As a beginner of research, I have learned a lot of knowledge, attitude and different view point from them.

Furthermore, I wish giving my thanks to other friends in our Department, Young-seob Kim, Jun-min Jang, Seung-dong Seo, Jae-hoon Jeong, Jun-seob Kim, Jin-young Kim. During my master course, I have been able to share and talk with them about research and life and then, they have helped me I finish the degree of master.

At last, I want to send gratitude to manager Kyung Jo. As a manager of our department, she always takes care of a lot of works related with experimental, administration, assistance and so on. As a novice of worker, I have got a great deal of help from her. If she isn't, it might be harder my master course. Thanks again to Kyung Jo.

Once more, I want to express my thanks to everybody. I sincerely hope the happiness will be full in your life.

# Abstract in Korean

이번 연구에서는 전통적인 metal oxide 광촉매인 ZnO와 최근 각광받고 있는 비금속 광촉매인 g-$C_3N_4$로 혼성 광촉매를 제작하였다. 이때 가열하는 온도와 사용하는 전구체를 다르게 하며 이들 요소가 광촉매의 물성과 활성에 미치는 영향과, ZnO 존재 하에서 g-$C_3N_4$를 합성했을 때의 합성 과정에서 ZnO과 g-$C_3N_4$에서 일어나는 상호 작용을 조사하였다. 연구 결과, DCDA-CNZ의 경우에는 높은 온도에서 Dicyandiamide를 이용하여 중합할 경우, ZnO와 g-$C_3N_4$ 사이의 더 강한 상호작용을 유도하고, 각 혼성 광촉매는 다른 형태학적 구조를 나타냄이 확인되었다. DCDA-CNZ는 g-$C_3N_4$과 ZnO 사이의 강한 상호작용의 결과로 core-shell 구조를 형성하였다. DCDA-CNZ 내의 강한 상호작용은 점진적으로 Zn의 전자 밀도를 감소시킬 뿐만 아니라, 전자-정공 쌍의 재결합을 방해했고, 이는 온도가 높아질수록 강해졌다. 이와 다르게 urea와 thiourea를 사용한 혼성 광촉매의 경우에는 다공성의 g-$C_3N_4$가 만들어져 ZnO와 분리된 형태로 존재하는 것이 확인되었다. 이는 열축합중합 과정에서 기체 방출이 일어나 g-$C_3N_4$과 ZnO의 상호작용을 방해했기 때문이다. 메틸렌 블루의 광분해 실험에서는 dicyandiamide를 사용하여 500 ℃에서 제작한 g-$C_3N_4$/ZnO 혼성 광촉매가 가장 높은 효율을 보임이 확인되었다. 그러므로 g-$C_3N_4$/ZnO 혼성 광촉매에서 g-$C_3N_4$과 ZnO 사이의 강한 상호작용으로 형성된 core-shell 구조가 광촉매적 활성에 영향을 미친다고 결론지었다.

# Abstract in English

In this study, g-$C_3N_4$/ZnO composite photocatalysts were synthesized through a one-step facile method at various annealing temperatures with diverse precursors. Thiourea, urea, and dicyandiamide (DCDA) were used as g-$C_3N_4$ precursors. The prepared photocatalysts were analyzed using several characterization methods to investigate the effect of annealing temperatures and precursors on the structural and optical properties and the role of ZnO during the thermal polycondensation process. Consequently, the higher annealing temperatures for DCDA-CNZ induced the stronger interaction between ZnO particles and g-$C_3N_4$ and each composite is composed of different morphological structures. The composite materials prepared from DCDA formed a core–shell structure with thin g-$C_3N_4$ layers caused by a strong interaction between DCDA and ZnO. The strong interaction in a core-shell g-$C_3N_4$/ZnO structure not only gradually decreased the electronic density of Zn but also proportionally inhibited the recombination of photo-generated electron-hole pairs, with increasing the annealing temperature. Meanwhile, thiourea and urea induced a segregated morphology of porous g-$C_3N_4$ and ZnO in the composites, which was ascribed to the weak interaction between them and gas generation during thermal polymerization. Furthermore, the photocatalysts prepared by DCDA at 500 ℃ exhibited the highest efficiency for the photocatalytic degradation of methylene blue under visible-light irradiation. Thus, in g-$C_3N_4$/ZnO composite materials, a core–shell morphology due to the efficient interaction between g-$C_3N_4$ and ZnO influenced photocatalytic activity.

# Contents

# Figure list

# Table List

# 1. Introduction

## 1.1. Photocatalyst

As the global energy crisis and environmental pollution are challenges to human society, the necessity to develop alternative means of energy production and pollutant elimination has continuously grown.[1-4] In recent years, extensive efforts have been made to explore high efficiency of visible-light photocatalysts due to their potential environment applications and solar energy utilizations.[5-7] Among the diverse strategies to enhance the photoconversion under visible-light irradiation, the combination of inorganic materials with graphitic carbon nitride (g-$C_3N_4$) as heterojunctioned composite materials is considerably attractive.

## 1.2. Carbon nitride

g-$C_3N_4$ has been reported as a metal-free polymeric semiconductor photocatalyst with high thermal and chemical stability as well as good electronic and optical properties.[5,8] The bandgap (~2.7 eV) is appropriate for visible-light irradiation. However, the use of single g-$C_3N_4$ photocatalysts has been limited due to their high electron-hole recombination and low specific surface area.[9-11] To overcome these obstacles, many researchers have tried to fabricate composite photocatalysts by combining g-$C_3N_4$ with inorganic semiconductors.[9,12] For example, g-$C_3N_4$/$TiO_2$ composites have been reported as excellent photocatalysts under visible-light irradiation.[9,13] ZnO, another famous single photocatalyst, has also been widely used as an inorganic component in composite photocatalysts.[12,14] Because of the wide bandgap of ZnO, a single ZnO material has the limitation to be photocatalytically activated under UV light irradiation.[14,15] When ZnO is combined with g-$C_3N_4$ as a composite photocatalyst, the g-$C_3N_4$/ZnO composite materials improved the photocatalytic activity under visible-light irradiation due to the formation of a Z-scheme heterojunction between g-$C_3N_4$ and ZnO, which can promote electron-hole separation.[16-20]

### 1.3. Annealing temperature

The optical and structural properties of g-$C_3N_4$-based composite materials depend on the annealing temperatures of the composite materials.[9,21,22] Li et al. reported that the g-$C_3N_4$/$TiO_2$ heterojunction prepared by the simple calcination of bulk g-$C_3N_4$ and $TiO_2$ at 600 ℃ showed better photocatalytic activity due to the influence of annealing temperatures on the g-$C_3N_4$ structure as well as the electron-hole separation in the composite materials.[9] Additionally, even in the simple preparation of g-$C_3N_4$/$TiO_2$ composites from a mixture of melamine and a titanium precursor, the heating temperature had a great influence on the structure, surface area and properties of the g-$C_3N_4$/$TiO_2$ composites.[21,22] The enhanced photocatalytic activity of the g-$C_3N_4$/$TiO_2$ composites at a specific treatment temperature might be related to the favorable structure and photocatalytic properties caused by the different thermal treatment temperatures.

### 1.4. Precursor

In order to prepare g-$C_3N_4$, nitrogen-rich precursors such as urea, thiourea, and dicyandiamide (DCDA) are usually used.[11,23-25] g-$C_3N_4$ precursors are one of the important factors influencing the morphological and optical properties of g-$C_3N_4$ and the interaction between g-$C_3N_4$ precursors and ZnO.[26,27] Dong et al. described that the photocatalytic activity and properties of g-$C_3N_4$ are depends on the sort of precursors and the amounts of sodium nitrate.[26] Truc and Shin investigated the thermal polymerization from diverse g-$C_3N_4$ precursors on $NiTiO_3$ inorganic particles.[27] Depending on the precursors, the morphological structure of the composites was different from each other, resulting in various photocatalytic behaviors.

### 1.5. Objective of this study

To the best of our knowledge, there have been no reports of the thermal treatment temperature and precursor effect on properties of g-$C_3N_4$/ZnO composite materials, yet. Therefore, the main goal of this study is investigation the optical and structural properties of the composites in addition to investigation of how interact g-$C_3N_4$ and ZnO particles during thermal polymerization process. To achieve that goals, we prepared various g-$C_3N_4$/ZnO (CNZ) composite materials by

a one-step facile method at different annealing temperatures and different, and then the prepared composites were characterized.

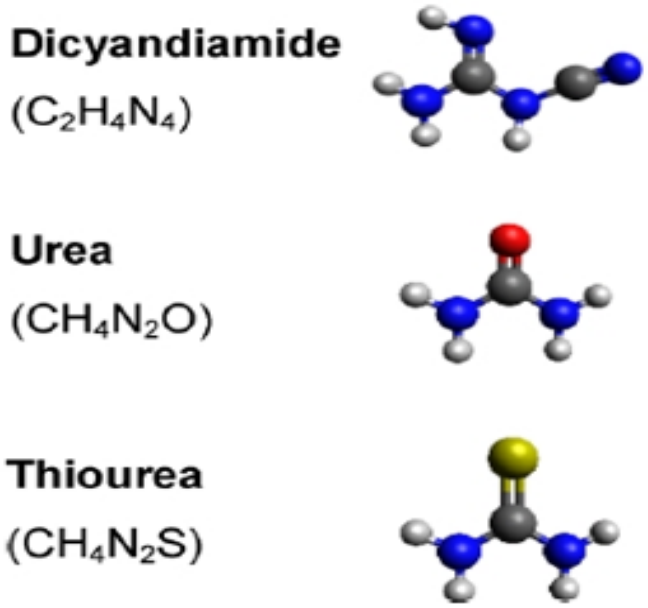


**Figure 1.1.** Molecular structures of Thiourea, Urea, and Dicyandiamide.[11]

# 2. Experimental

## 2.1. Catalyst preparation

### 2.1.1. Annealing temperature

The chemicals used in this study, such as zinc oxide, thiourea, urea, and DCDA, were purchased from Sigma-Aldrich Korea (Gyeonggi, South Korea). In order to prepare the composites, 0.2 g of ZnO and 0.2 g of DCDA were mixed and ground together in a mortar to facilitate complete mixing. The mixed samples were placed in a crucible and moved to a tubular furnace. Under $N_2$ flow, the powders were heated to a certain temperature (T = 350, 400, 450, and 500 ℃) with a ramping rate of 10 ℃/min and then were maintained at 500 ℃ for 4 h. The obtained powders were washed with DI water using a centrifuge for five times. The washed solid samples were dried in an oven for 12 h. The final solid products were designated as CNZ-T (T = 350, 400, 450, and 500) according to the annealing temperatures. For comparison, pure g-$C_3N_4$ was also produced by thermal treatment of DCDA in a tubular furnace under $N_2$ flow at 550 ℃.

### 2.1.2. Precursor

The materials used in this study, such as zinc oxide, thiourea, urea, and DCDA, were purchased from Sigma-Aldrich Korea (Gyeonggi, South Korea). Here, 0.2 g of ZnO and 0.2 g of precursors (urea, thiourea, and DCDA) were ground together in a mortar for 10 mins. The mixed powders were placed in a crucible and moved to a tubular furnace. Under $N_2$ atmosphere, the samples were heated up to 500 ℃ with a ramping rate of 10 ℃/min and then were maintained at 500 ℃ for 4 h. The following steps were same as in case of annealing temperature effect. The obtained samples were designated as P- CNZ (P = Thio, Urea, DCDA) depending on the g-$C_3N_4$ precursors.

## 2.2. Catalyst characterization

In this study, the annealing temperatures for each composite material and the amounts of g-$C_3N_4$ in the Composites were determined *via* thermogravimetric analysis (TGA, TGA Q50, TA instruments, USA). The crystalline structures of each phase were analyzed by an X-ray diffraction spectrometer (XRD, Rigaku D/MAZX 2500 V/PC high-power diffractometer, Japan / Cu Kα, λ=1.5415Å) with a scan rate of 2°/min. The morphologies of the composites were analyzed using a field-emission scanning electron microscope (FE-SEM, JSM-600F, JEOL, Japan) and a high-resolution transmission electron microscope (HR-TEM, JEM-2100F, JEOL, Japan). The specific surface area was determined by employing a $N_2$ adsorption-desorption technique (ASAP 2020, Micromeritics, USA) and the BET equation. The chemical and optical properties of the composites including surface functional groups, recombination rate, and chemical states were analyzed using a FTIR spectrometer (Nicolet 380, Thermo Electron Co., USA), UV-vis spectrophotometer (Spectra Max Plus 384, Molecular Devices, USA), a photoluminescence (PL) spectrometer with a 473 nm diode laser (G9800A, Agilent Technologies, USA), and an X-ray photoelectron spectrometer (K-Alpha, Themo Fisher Scientific Co., USA)

## 2.3. Photocatalytic reaction test

Here, 10 mg of CNZ photocatalyst was immersed in a beaker containing 50 mL of methylene blue (MB, 10 ppm) aqueous solution. The beaker was placed on a stirrer with a magnetic bar, and the solution was continuously stirred in the dark for 60 min to achieve equilibrium adsorption. Subsequently, photocatalytic degradation of MB was performed under visible-light irradiation from four surrounding light sources (model GB22100(B)EX-D Eltime, 100 W, $\lambda_{max}$ = 545 nm) for 90~120 min. Here, 1 mL of MB solution was collected from the beaker through a syringe and PTFE syringe filter (0.2 μm, Φ 13 mm). Then, the absorbance spectrum of the solution was measured using a UV–vis spectrometer.

# 3. Results and Discussions

## 3.1. Annealing temperature effect

### 3.1.1. Structural and Morphological analysis

DCDA was used as a precursor to participate in the thermal polymeric condensation chain for conversion into melamine, melam, melem, melon, and eventually g-$C_3N_4$ structure.[28-30] The temperature-programmed weight loss was monitored by TGA under $N_2$ flow to understand the thermal formation behavior of the composites. Firstly, the TGA and DTGA profiles of DCDA and as-prepared DCDA-ZnO were plotted to simply simulate the thermal formation of the g-$C_3N_4$ structure with or without ZnO (**Fig. 3.1A**). The DTGA profile of DCDA shows five weight loss peaks in the thermal formation process of the g-$C_3N_4$ structure, corresponding to four formation steps of the g-$C_3N_4$ structure and the last decomposition step of g-$C_3N_4$: melamine to melam (254 ℃), melam to melem (332 ℃), melem to melon (381 ℃), melon to g-$C_3N_4$ (550–650 ℃), and the decomposition of g-$C_3N_4$ (ca. 700 ℃), respectively. Meanwhile, in the DTGA profile of as-prepared DCDA-ZnO, four weight loss peaks were observed and all of the peak positions were shifted to lower thermal polymeric condensation temperatures: melamine to melam at 207 ℃, melam to melem and melon at 307 ℃, melon to g-$C_3N_4$ between 350–500 ℃, and the decomposition of g-$C_3N_4$ around 520 ℃, which indicates that the presence of ZnO facilitates the thermal formation of the g-$C_3N_4$ structure at lower temperatures as a result of interactions between ZnO and the precursors of g-$C_3N_4$. The thermal formation behaviors of g-$C_3N_4$ in g-$C_3N_4$/$TiO_2$ and g-$C_3N_4$/$NiTiO_3$ composite materials were similar where the presence of $TiO_2$ or $NiTiO_3$ inorganic phase promoted the formation of melon or g-$C_3N_4$ structure at lower temperatures.[22,30] Based on the TGA results, the composites in this study were prepared at 350, 400, 450, and 500 ℃, which are below the temperatures of g-$C_3N_4$ decomposition.

**Figure 3.1B** exhibits the TGA and DTGA profiles of the composites. All of TGA profiles of the composites were very similar in spite of the different annealing temperatures. The compositions of g-$C_3N_4$ and ZnO in the composites were similar although the CNZ photocatalysts were thermally treated at different annealing temperatures. The contents measured by the TGA analysis are listed in **Table 3.1**, indicating very similar g-$C_3N_4$ contents (25.9–28.8%). For comparison, the TGA and DTGA profiles of g-$C_3N_4$ are also shown in **Fig. 3.1B**. In the DTGA profile of g-$C_3N_4$, an asymmetric sharp decomposition peak appeared at 685 ℃, reflecting the strong formation of an interlayered g-$C_3N_4$ structure with weak shoulders. However, in the DTGA profile of the composites, two broad decomposition peaks were detected in the ranges of 400–600 ℃ and 600–700 ℃. The g-$C_3N_4$ in the composites was composed of at least two g-$C_3N_4$ structure types: a less polymerized g-$C_3N_4$ structure and an interlayered g-$C_3N_4$ structure.

**Table 3.1.** Physicochemical properties of the CNZ composites.

| Sample | $S_{BET}$ ($m^2$/g)* | $R_{N1s}$** | ZnO crystallite size (nm)*** | Contents (%)**** | |
|---|---|---|---|---|---|
| | | | | $C_3N_4$ | ZnO |
| ZnO | 5.84 | - | 47.9 | 0 | 100 |
| CNZ-350 | 6.55 | 1.24 | 46.9 | 27.3 | 72.7 |
| CNZ-400 | 2.20 | 0.99 | 43.2 | 27.6 | 72.4 |
| CNZ-450 | 2.02 | 0.99 | 38.9 | 28.8 | 71.2 |
| CNZ-500 | 1.58 | 0.60 | 43.6 | 25.9 | 74.1 |
| g-$C_3N_4$ | 24.21 | 3.67 | - | 100 | 0 |

** The values are specific BET surface areas determined by the $N_2$ adsorption/desorption technique.*

*** The intensity ratios of $sp^2$-bonded N atoms (C-N=C) to amino functional groups (-NH) were calculated based on the fitted curves of XPS N 1s data.*

**** The values were calculated using the Scherrer equation.*

***** The values were calculated from TGA measurements.*

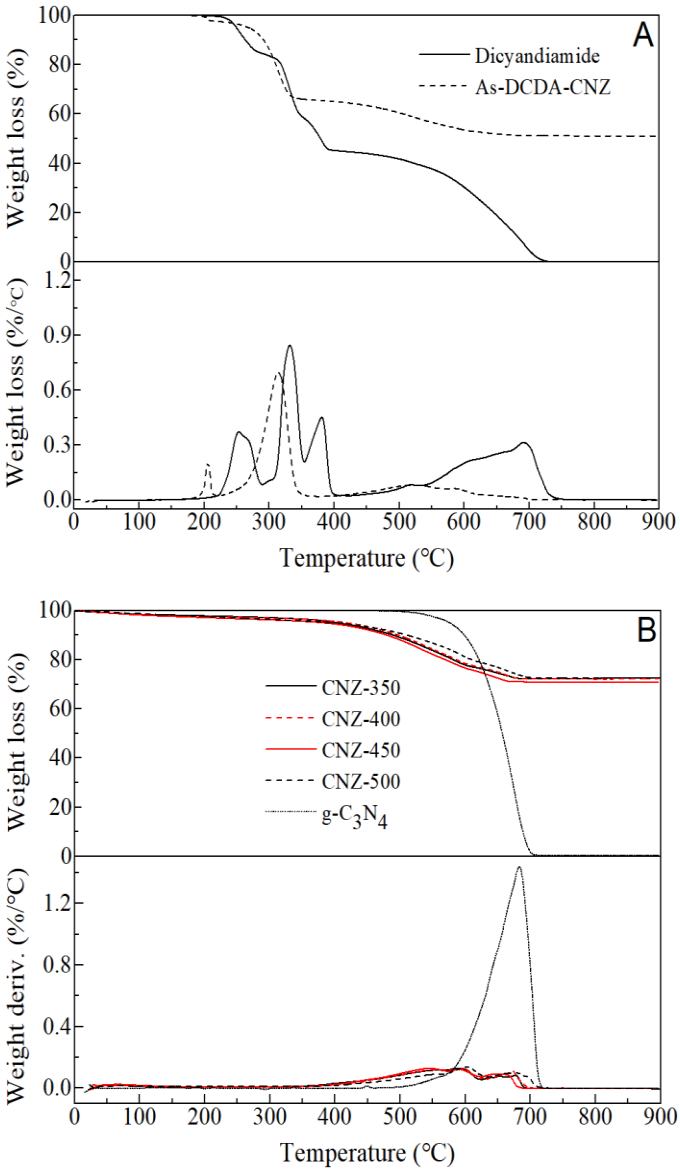


**Figure 3.1.** TGA and DTGA profiles of (A) Dicyandiamide and As-DCDA-ZnO and (B) CNZ-350, 400, 450, and 500 with g-$C_3N_4$.

XRD was employed to analyze the crystallinity of g-$C_3N_4$ and ZnO in the composite materials. **Figure 3.2A** displays the XRD patterns of composites and their individual components. The characteristic peak of g-$C_3N_4$ shows a strong characteristic peak at $2\theta = 27.07°$, representing the stacking of conjugated π-π in aromatic units of graphitic carbon nitride (**Fig. 3.2A(a)**), which matches the (0 0 2) diffraction plane and d-spacing $d_{(002)} = 0.329$ nm corresponding to the distance between layers.[32-33] Meanwhile, the characteristic peaks for ZnO phase with a $P6_3mc$ space group (JCPDS No. 36-1451) are also observed at 31.8°, 34.4°, 36.3°, 47.5°, 56.7°, and 62.9° in the XRD patterns of the composites (**Fig. 3.2A(b-e)**).[28,29] The peak positions of ZnO phase were not shifted and no additional phase was generated on all samples. The narrow and sharp peaks of ZnO phase were observed even at high annealing temperatures, demonstrating the high crystallinity of the ZnO particles. The ZnO crystallite sizes in the composites were calculated by the Scherrer equation and were in the range of 38.9–47.9 nm (**Table 1**). However, the characteristic XRD peaks for g-$C_3N_4$ were not detected in the composites (**Fig. 2A(b-e)**). The characteristic XRD peak for the g-$C_3N_4$ disappeared in the composites even though the g-$C_3N_4$ contents were still over 25%, which is not consistent with results reported previously.[17-19] In previous studies, g-$C_3N_4$/ZnO composite materials were synthesized by a hydrothermal method using g-$C_3N_4$ and ZnO which were separately prepared. In this study, alternatively, the composites were fabricated by a one-step facile method using DCDA with ZnO under temperature-programmed conditions, resulting in high dispersion of amorphous g-$C_3N_4$ structure over ZnO particles.[20,30] This is in good agreement with the TGA results regarding the amorphous g-$C_3N_4$.

FTIR spectra of the composites and their individual components were obtained to investigate the interaction between g-$C_3N_4$ and ZnO (**Fig. 2B**). The FTIR bands in the range of 1200–1650 $cm^{-1}$ correspond to typical stretching modes of carbon nitride aromatic rings.[19] The bands at 1241 $cm^{-1}$, 1323 $cm^{-1}$ and 1410 $cm^{-1}$ are assigned to the vibration modes of aromatic C-N in the structure. The peaks at 1564 $cm^{-1}$, and 1642 $cm^{-1}$ correspond to C=N stretching of the tri-s-triazine ring in the g-$C_3N_4$ structure. The sharp band at 807 $cm^{-1}$ is assigned to out of plane bending of s-triazine units, which can be considered as a main peak representing the existence of

g-$C_3N_4$. For the composites, all of the FTIR spectra are similar for the different annealing temperatures with a sharp band at 807 $cm^{-1}$ and stretching bands around 1200–1650 $cm^{-1}$ for the g-$C_3N_4$ structure. Accordingly, the tri-s-triazine ring structure of g-$C_3N_4$ in the composites was well developed at all the annealing temperatures. However, the band at 807 $cm^{-1}$ was slightly shifted to a lower band position with increasing annealing temperature for the composites (dashed line in **Fig. 2B**). Wang et al. also observed a red shift of the main characteristic bands of the g-$C_3N_4$ structure in the core-shell g-$C_3N_4$/ZnO composite materials, and suggested not only the possible formation of chemical bonds but also the interfacial charge transfer between g-$C_3N_4$ and ZnO.[18] Similarly, in this study, the strong interaction between ZnO and g-$C_3N_4$ might be weakened the bonding strength of C-N and C=N of the amorphous g-$C_3N_4$ in the composites, implying the interfacial charge transfer as well as the chemical bond formation between ZnO and amorphous g-$C_3N_4$.

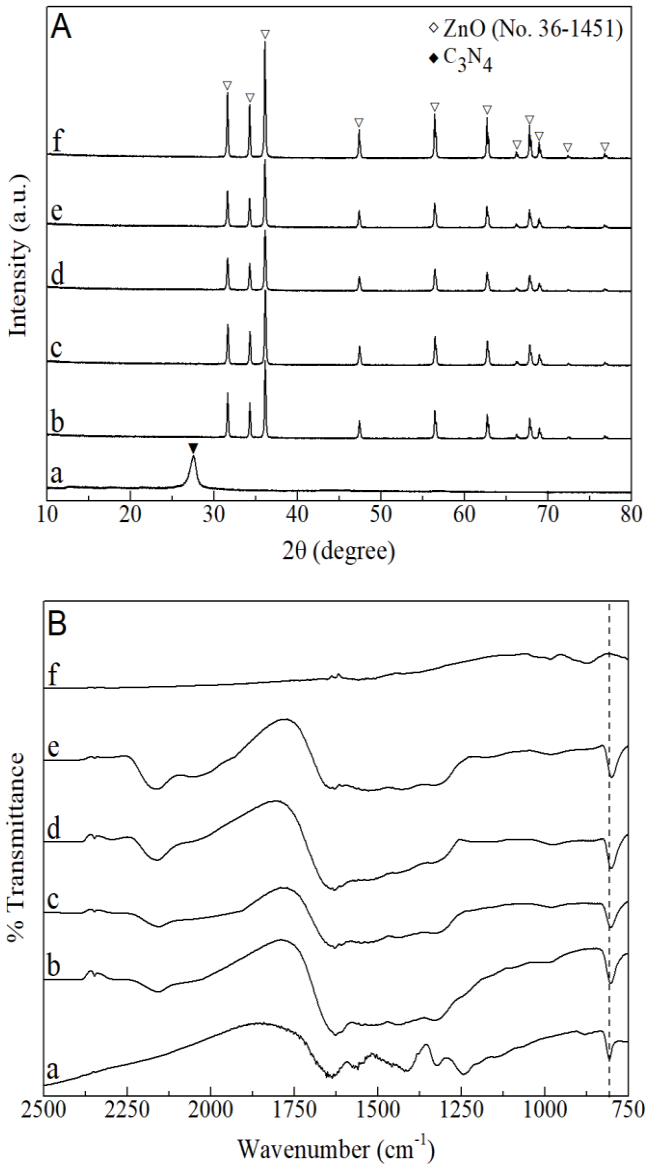


**Figure 3.2.** (A) XRD patterns and (B) FTIR spectra of (a) g-$C_3N_4$, (b-e) CNZ-350, 400, 450, and 500, and (f) ZnO.

The morphology of the composites was analyzed *via* field emission scanning electron microscopy. Pure g-$C_3N_4$ was composed of irregular particles (**Fig. 3.3(b)**). For the composites, as a whole, their morphologies were very similar irrespective of the annealing temperature with simple development of particle aggregates over lamellar-structured particles (**Fig. 3.3(c-f)**).

**Figure 3.4** shows high resolution TEM images of the composites. TEM images of ZnO were obtained and the FFT pattern analysis for the ZnO was additionally conducted to prove the existence of the ZnO phase in composites (**Fig. 3.4**). Interestingly, thin layers of amorphous g-$C_3N_4$ structure were detected around the ZnO particles, reflecting the thermal formation of less polymerized g-$C_3N_4$ in a core-shell structure of the composites (**Fig. 3.4(a,c)**). The interaction between ZnO and the intermediates of g-$C_3N_4$ occurring during the thermal formation resulted in thin layers of amorphous g-$C_3N_4$ instead of interlayers of the g-$C_3N_4$ structure.

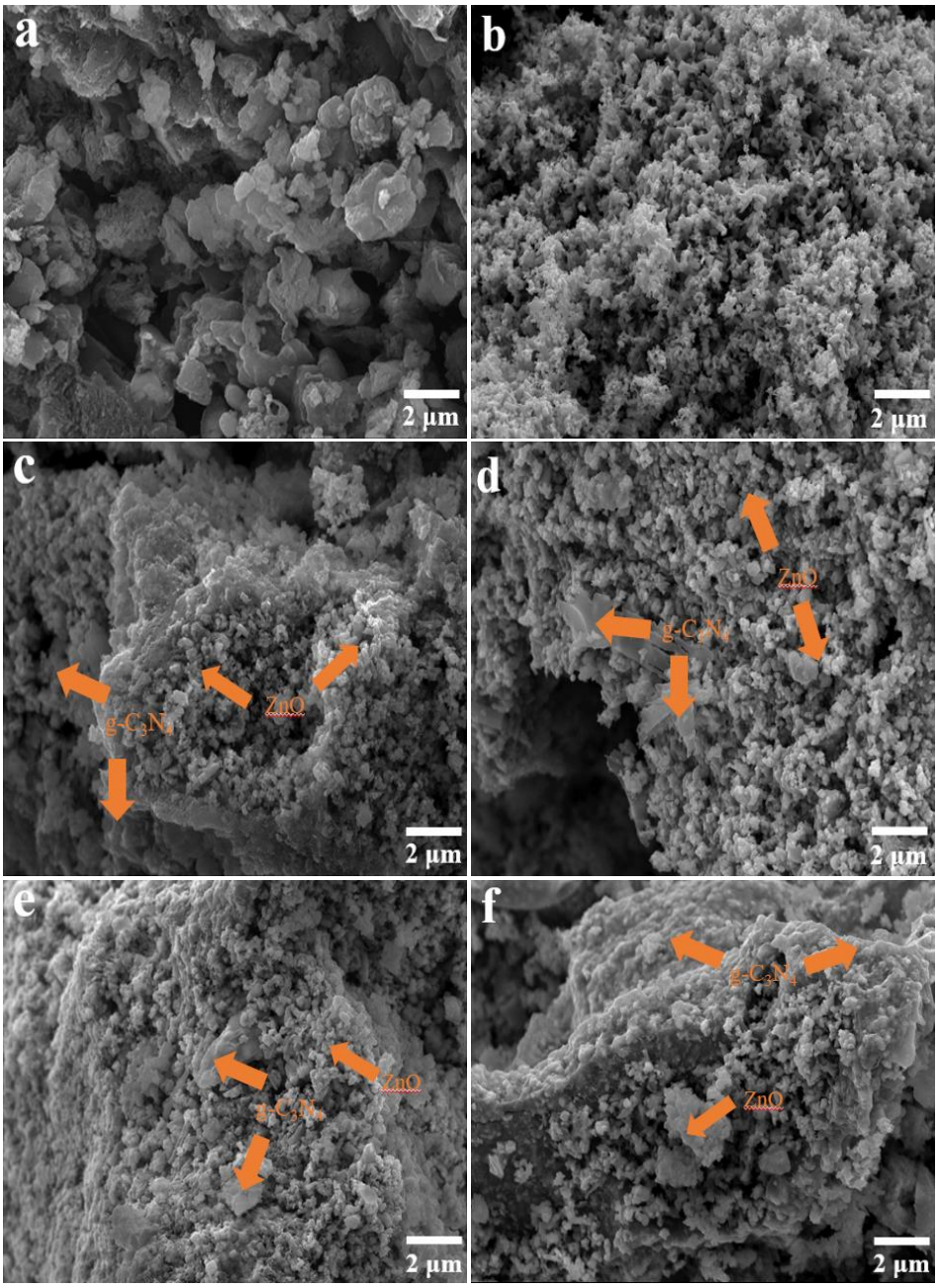


**Figure 3.3.** FE-SEM images of (a) g-$C_3N_4$, (b) ZnO, and (c-f) CNZ-350, 400, 450, and 500.

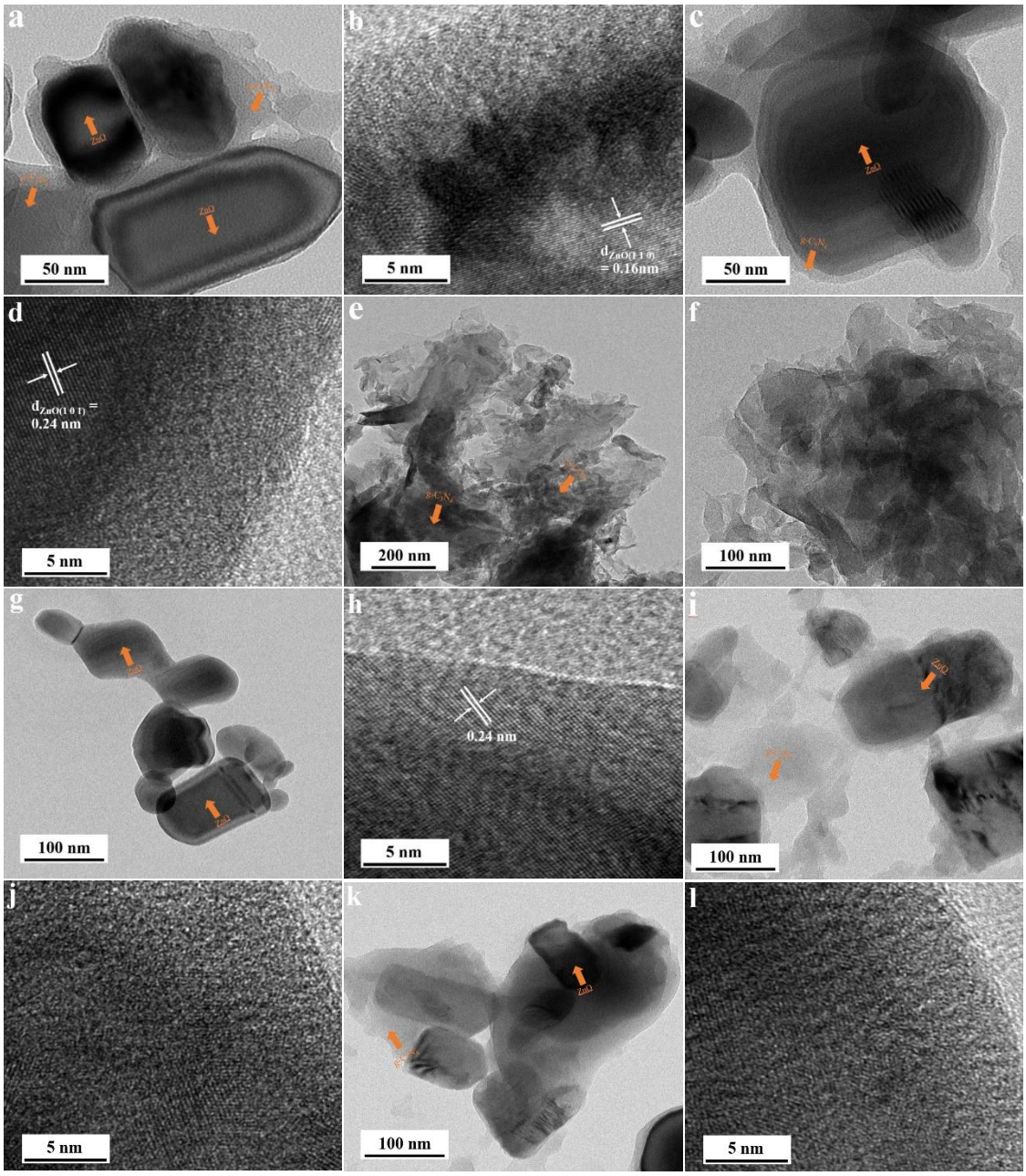


**Figure 3.4.** HR-TEM images of (a,b) CNZ-350, (c,d) CNZ-450, (e,f) g-$C_3N_4$, (g,h) ZnO, (i,j) CNZ-400, and (k,l) CNZ-500.

### 3.1.2. Electronic and Optical Properties.

XPS analysis was employed to investigate the chemical states of Zn, O, C, and N elements in the composites. The XPS data for C 1s and its fitted curves are plotted in **Fig. 3.5A**. The peaks deconvoluted at 284.6, 287.4, and 288.8 eV in the C 1s spectrum can be assigned to graphitic carbon (C–C), carbon atoms bonded to the $–NH_2$ group, the $sp^2$-bonded carbon inside the aromatic group (N-C=N), and oxygenated carbon (C=O), respectively.[36-42] The relative intensity of the carbon atoms bonded to the g-$C_3N_4$ structure (C–$NH_2$, N–C=N, C=O) to graphitic carbon (C–C) increased compared to that of g-$C_3N_4$, which implies less polymerization of the g-$C_3N_4$ structure in the composites. **Figure 3.5B** shows the XPS results of N 1s along with fitted curves. Each fitted curve can be assigned as $sp^2$-bonded nitrogen (C–N=C), tertiary nitrogen (N–$(C)_3$), and amino functional groups in the aromatic ring (–NH) with binding energies of 397.8, 398.8, and 399.8 eV, respectively.[36-43] The binding energies and intensities of the fitted curves in XPS N 1s data are listed in **Table 3.2**. Here, we calculated the intensity ratios of the $sp^2$-bonded nitrogen atoms in g-$C_3N_4$ aromatic rings (C-N=C) to the amino functional groups in the aromatic ring (-NH) to compare the degree of polymerization of the g-$C_3N_4$ structure. The calculated values ($R_{N1s}$) are listed in **Table 3.1**. The $R_{N1s}$ value of g-$C_3N_4$ (3.57) is much higher than those (0.60–1.24) of the composites, indicating that the g-$C_3N_4$ structure in the presence of ZnO was less polymerized than without ZnO. This is consistent with the XRD and TGA results revealing amorphous g-$C_3N_4$ structure for the composites and interlayered crystalline g-$C_3N_4$ structure for g-$C_3N_4$. The reduced thermal polymerization of the g-$C_3N_4$ structure over the composites was caused by the interaction between ZnO and the intermediates of g-$C_3N_4$ in the thermal formation process. In addition, the $R_{N1s}$ for composites values gradually decreased with increasing the annealing temperature, implying the stronger interaction in the core-shell structure at the higher annealing temperature.

The XPS data of Zn $2p_{3/2}$ and O 1s are presented in **Fig. 3.6A and 3.6B**, respectively. The Zn $2p_{3/2}$ binding energies of composites were blue-shifted from 1021.3 to 1021.9 eV with increasing annealing temperatures, demonstrating that the electron density of Zn decreased (**Fig. 3.6A**). Sun

et al. suggested that the blue shift in Zn $2p_{3/2}$ binding energy can be attributed to the formation of N-Zn bonding in the g-$C_3N_4$/ZnO composites.[42] Similarly, in this study, the strong interaction between ZnO and g-$C_3N_4$ induced the electron-deficient of Zn with at higher annealing temperature. The O 1s spectra of ZnO can be deconvoluted into the lattice oxygen of ZnO at 530.1 eV and surface hydroxyl groups (-OH) at 531.6 eV (**Fig. 3.6B**).[37-39] For the composites, the peak position of the lattice oxygen of ZnO was shifted from 530.1 to 530.9 eV, and the peak position of the surface hydroxyl groups (-OH) was shifted from 531.6 to 532.4 eV (**Fig. 3.6B**). The binding energies and intensities of each fitted peak in the XPS O 1s data are listed in **Table 3.3**. Feng et al. explained that the shift of O 1s in the ZnO/g-$C_3N_4$ composite materials to a higher binding energy was attributed to the migration of electrons from ZnO to g-$C_3N_4$.[16] In the same way, the O 1s peak shift in the composites was ascribed to electron migration from ZnO to the g-$C_3N_4$ structure, which is also evidenced for the interaction between ZnO and the amorphous g-$C_3N_4$. Additionally, a sharp band at 807 $cm^{-1}$ in FTIR spectra, which corresponds to a bending motion of s-triazine units, shifted to a lower wavenumber with increasing annealing temperature. The red shift of this band might be caused by the interaction with the ZnO particles.

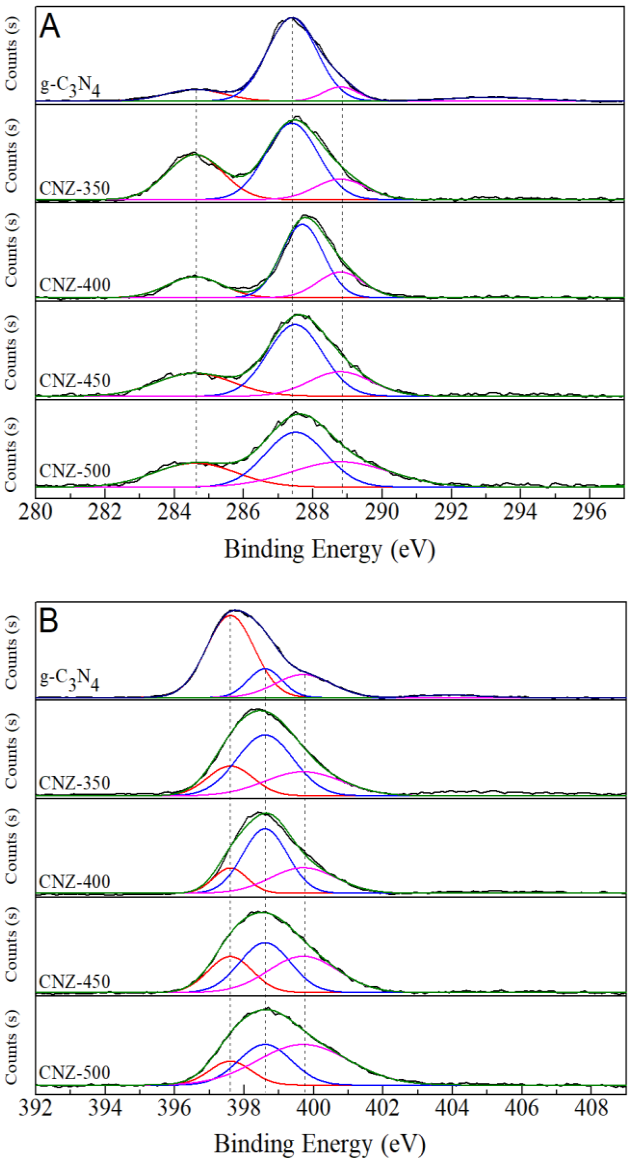


**Figure 3.5.** XPS data of (A) C 1s and (B) N 1s of (a) g-$C_3N_4$, (b-e) CNZ-350, 400, 450, and 500.

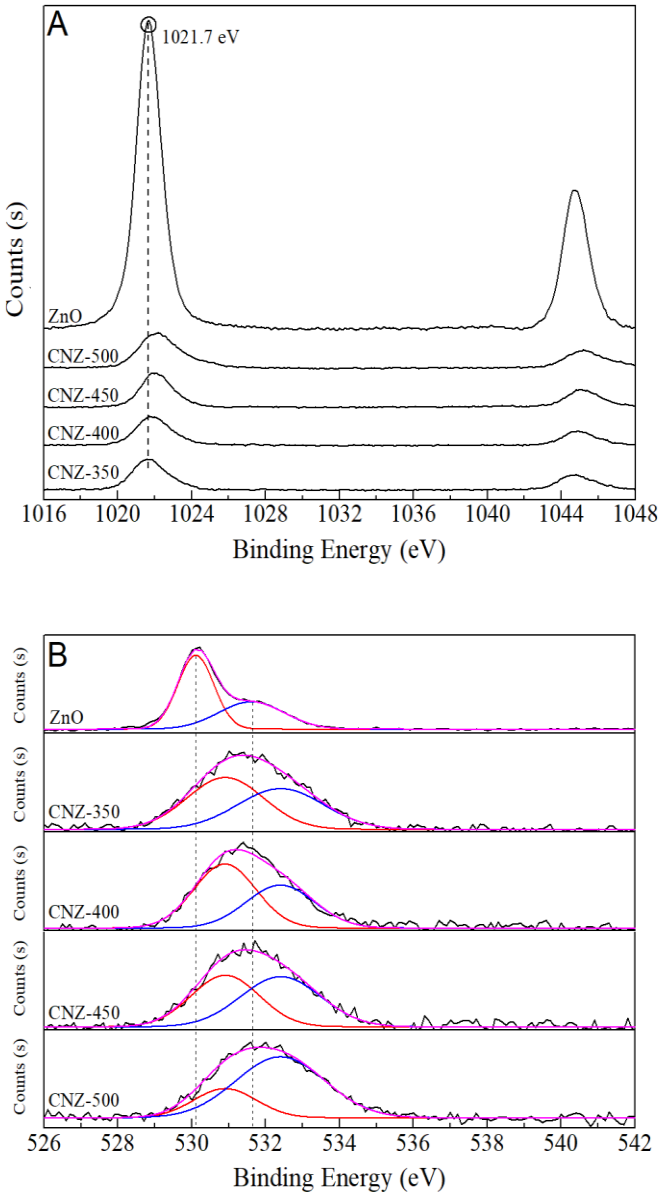


**Figure 3.6.** XPS data of (A) Zn 2p and (B) O 1s of (a) ZnO and (b-e) CNZ-350, 400, 450, and 500.

**Table 3.2.** The binding energies and intensities of the fitted curves in the XPS N 1s data.

| Sample | Peak 1 position (eV) | Peak 1 intensity | Peak 2 Position (eV) | Peak 2 intensity | Peak 3 position (eV) | Peak 3 Intensity |
|---|---|---|---|---|---|---|
| g-$C_3N_4$ | 397.6 | 9487.4 | 398.6 | 3322.3 | 399.7 | 2658.3 |
| CNZ-350 | 397.6 | 2194.3 | 398.6 | 4478.6 | 399.7 | 1772.4 |
| CNZ-400 | 397.6 | 2285.6 | 398.6 | 5572.9 | 399.7 | 2307.2 |
| CNZ-450 | 397.6 | 1963.4 | 398.6 | 2688.3 | 399.7 | 1983.3 |
| CNZ-500 | 397.6 | 1277.7 | 398.6 | 2121.7 | 399.7 | 2117.2 |

**Table 3.3.** The binding energies and intensities of the fitted curves in the XPS O 1s data.

| Sample | Peak 1 position (eV) | Peak 1 intensity | Peak 2 Position (eV) | Peak 2 intensity |
|---|---|---|---|---|
| ZnO | 530.1 | 13382.9 | 531.6 | 5072.9 |
| CNZ-350 | 530.9 | 1255.7 | 532.4 | 999.7 |
| CNZ-400 | 530.9 | 1379.5 | 532.4 | 957.6 |
| CNZ-450 | 530.9 | 853.3 | 532.4 | 833.0 |
| CNZ-500 | 530.9 | 530.9 | 532.4 | 1298.5 |

**Figure 3.7A** shows PL spectra of the composites, ZnO, and g-$C_3N_4$. Firstly, the PL intensities of the composites decreased proportionally with increasing annealing temperatures, which indicates that the photo-generated electron-hole recombination is much more inhibited in the composites prepared under higher temperature conditions. That is, the lowest PL intensity of CNZ-500 implies the slowest recombination rate among the composites. Secondly, with increasing annealing temperature, the peak positions of the maximum PL intensities for the composites were red-shifted. In the inset of **Fig. 3.7A**, the normalized PL spectra apparently exhibit a red shift of the PL peaks. The maximum PL peak position of 412 nm for CNZ-350 was shifted to 441 nm for CNZ-500. In the literature, similar results over g-$C_3N_4$ were reported with a red shift of PL spectra with increasing annealing temperatures.[43,44] This phenomenon was explained by the enhancement of the π-conjugated system in the g-$C_3N_4$ with increasing the annealing temperatures, resulting in the red shift in the PL spectra. In this study, the enhancement of π-conjugated system in the g-$C_3N_4$ might be attributed to the electron migration from ZnO, which was proven in the XPS data and FTIR spectra. With increasing annealing temperatures, the electron density of the Zn in the composites decreased. Accordingly, the higher annealing temperature for the composites caused the stronger interaction between ZnO and g-$C_3N_4$, modifying the optical properties with a slow recombination rate in the composites and low electron density in Zn (**Fig. 3.7B**).

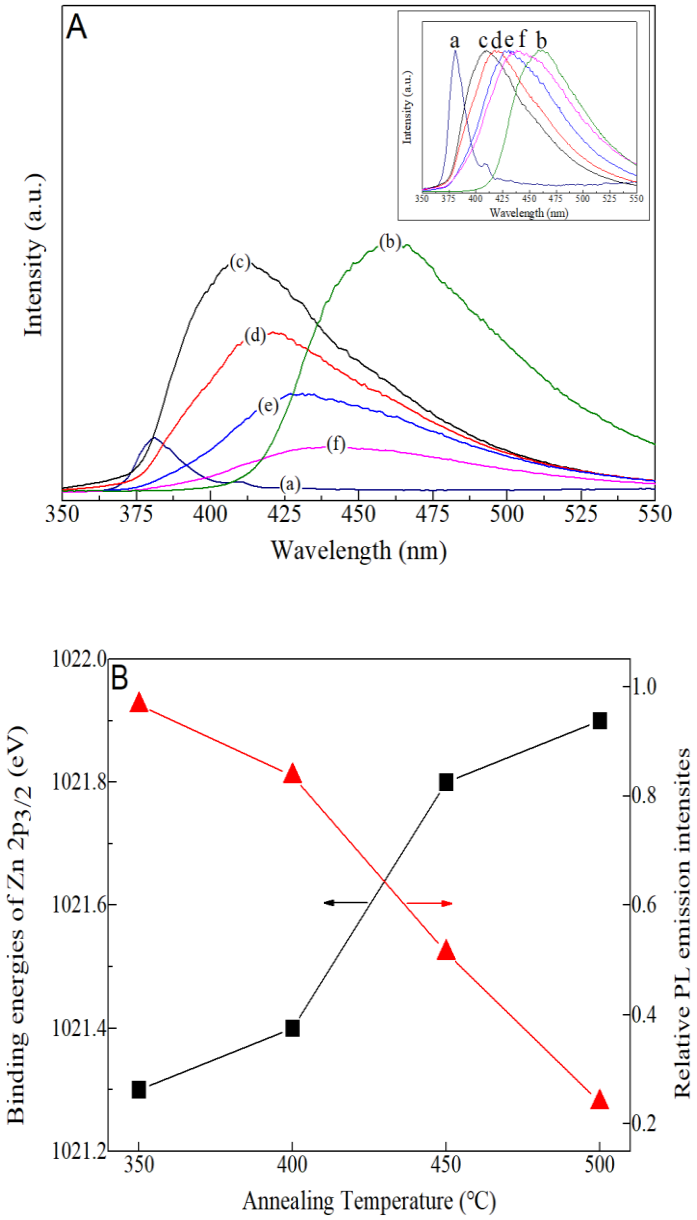


**Figure 3.7.** (A) Photoluminescence (PL) spectra of (a) g-$C_3N_4$, (b) ZnO, (c-f) CNZ-350, 400, 450, and 500 (the inset of (A) represents the normalized PL spectra) and (B) relative PL emission intensities and the PL emission peak positions as a function of annealing temperatures.

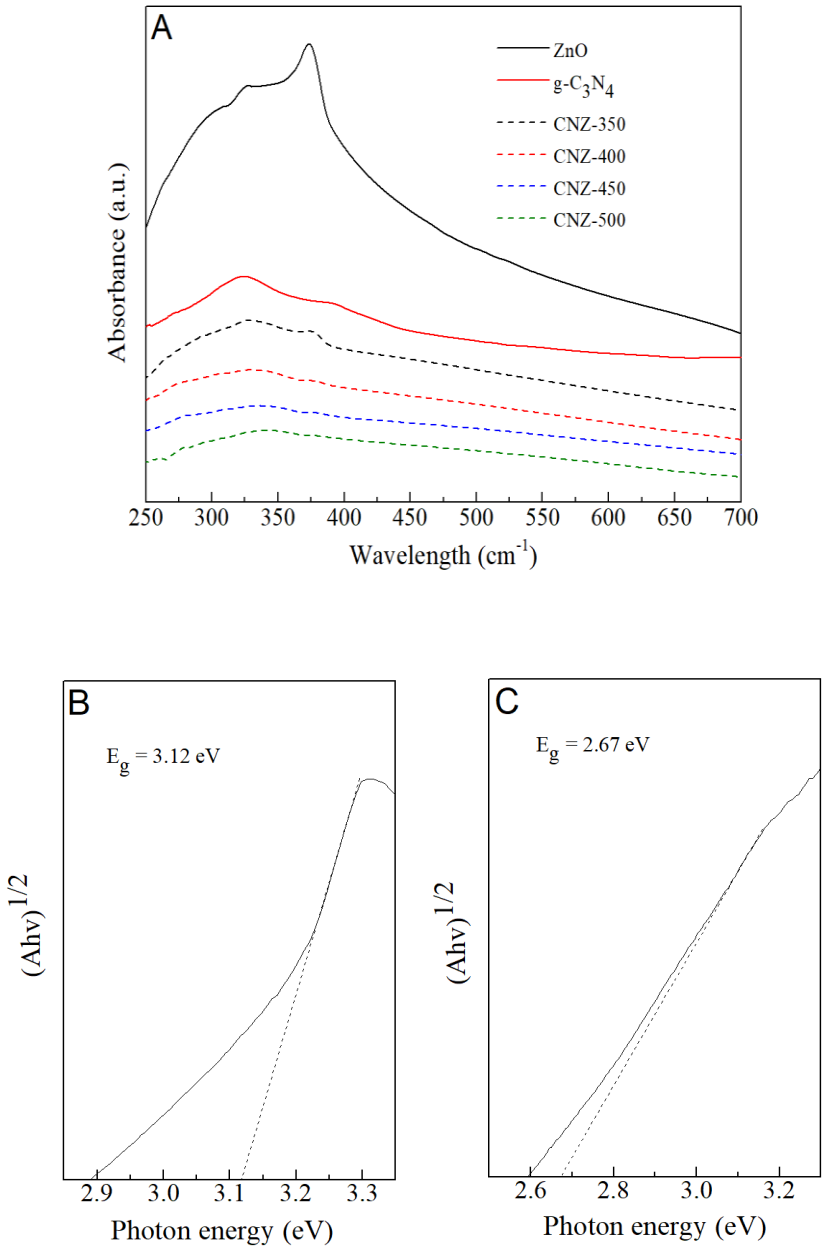


**Figure 3.8.** (A) UV-visible spectra of g-$C_3N_4$, ZnO and CNZ-350, 400, 450, and 500 and (B, C) Tauc plots of ZnO and g-$C_3N_4$.

### 3.1.3. Photocatalysis and Thermal Formation of Composites.

**Figure 3.9** represents MB photocatalytic degradation results of pure g-$C_3N_4$ and the composites under visible light irradiation. The correlation between photocatalytic activity and recombination rate of the composites with increasing annealing temperatures.

**Figure 3.10** shows a schematic illustration of the thermal formation of the g-$C_3N_4$ structure over ZnO particles. Without ZnO, DCDA was consecutively polymerized into melamine, melam, melem, melon, and g-$C_3N_4$ in the thermal polymerization process. In g-$C_3N_4$, an interlayered crystalline g-$C_3N_4$ structure was dominantly formed through the continuous extension of g-$C_3N_4$ network above 550 ℃. In contrast, in the presence of ZnO, the polymerization of DCDA occurred through the interaction with ZnO particles even below 500 ℃. As a result, ZnO particles were covered with thin layers of amorphous g-$C_3N_4$ due to the low degree of polymerization of the g-$C_3N_4$ network. Additionally, the interaction between ZnO and amorphous g-$C_3N_4$ decreased the electron density of Zn in the composites, which was evidenced by the XPS data. In the PL spectra, increasing the thermal treatment temperature of the composites induced a proportional decrease in the PL emission intensities as well as a red shift of the centered position of the PL peaks. This change in the optical property of the composites was also caused by the enhancement of π-conjugated system in the g-$C_3N_4$ due to the interaction between ZnO and amorphous g-$C_3N_4$. **Figure 3.11** displays a schematic illustration of the Z-scheme charge transfer model from ZnO to g-$C_3N_4$ in the composites. The formation of thin layers of amorphous g-$C_3N_4$ surrounding ZnO particles induced chemical bonds between ZnO and g-$C_3N_4$, resulting in the Z-scheme charge transfer (electron migration) from ZnO to g-$C_3N_4$. The composite material prepared at 500 ℃ (CNZ-500) showed the slowest recombination rate due to the optimal interaction between ZnO and g-$C_3N_4$, resulting in the highest activity for the photocatalytic MB degradation.

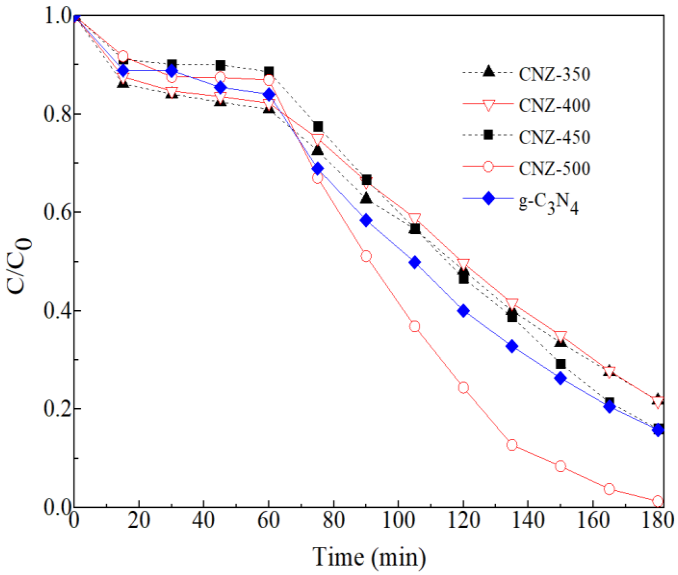


**Figure 3.9**. Photocatalytic degradation of methylene blue under visible light irradiation of g-$C_3N_4$, CNZ-300, 350, 400, and 500.

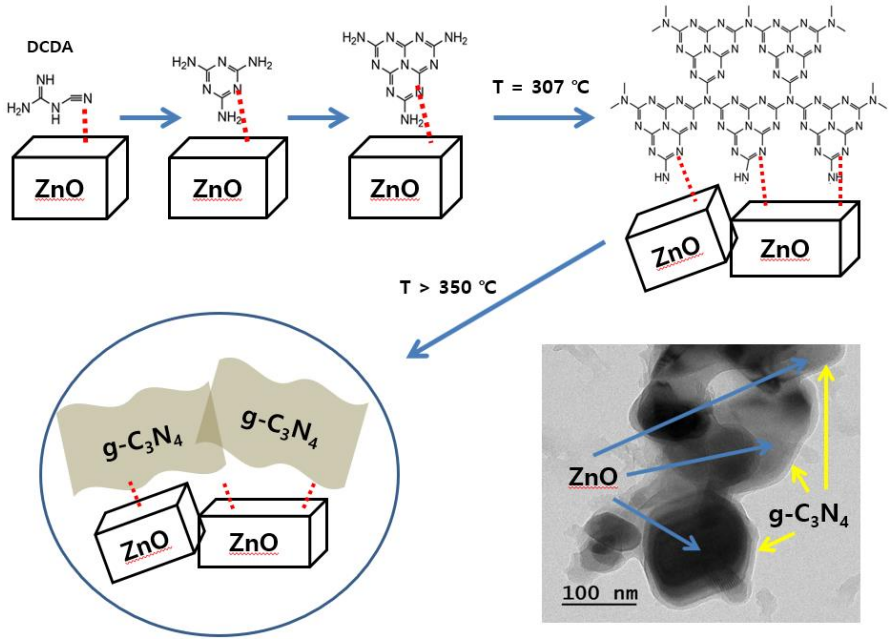


**Figure 3.10.** A schematic illustration of the interaction between ZnO and g-$C_3N_4$ in the thermal formation of the g-$C_3N_4$ structure in composites and a corresponding FE-SEM image.

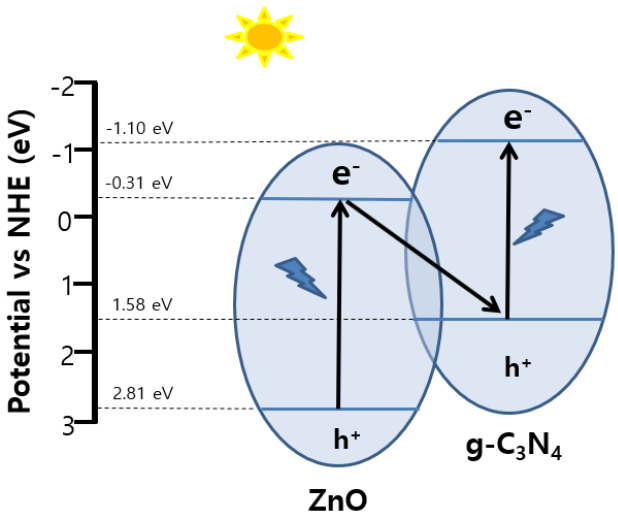


**Figure 3.11.** A schematic illustration of charge transfer (electron migration) from ZnO to g-$C_3N_4$.

## 3.2. Precursor effect

### 3.2.1. Structural and Morphological analysis

TGA and DTGA analyses were conducted to investigate the effect of ZnO on the thermal polymerization process for fabricating the CNZ composites under $N_2$ flow. Regardless of the g-$C_3N_4$ precursor types, the existence of ZnO affects the polymerization steps, resulting in the shift in polymerization temperatures. The polymerization temperatures of the CNZ composites become lower than those of pure precursors, as shown in **Figs. 12(A-C)**. This result implies that the existence of ZnO particles facilitates thermal polymerization through the interaction between the precursors and ZnO. Meanwhile, the amount of g-$C_3N_4$ in the CNZ composites was determined through the TGA measurement with air flow. Interestingly, despite the different TGA profiles of the As-prepared-CNZ, every CNZ composites contains a similar amount of g-$C_3N_4$. As listed in **Table 3.4**, the g-$C_3N_4$ contents for Thio, Urea, and DCDA–CNZ are 28.67%, 29.60%, and 26.97%, respectively. Thus, the interaction between g-$C_3N_4$ and ZnO is different from the interaction in g-$C_3N_4$/$NiTiO_3$ composites that contain 1.52%–23.23% of g-$C_3N_4$ contents, depending on the precursors.[27]

XRD was employed to investigate the crystalline structures of the CNZ composites. The XRD patterns of the CNZ composites are presented in **Fig. 3.13**. A peak at 28.42° is a characteristic peak for the stacking of conjugated π–π in aromatic units of g-$C_3N_4$.[46-47] The peaks observed at 31.8°, 34.4°, 36.3°, 47.5°, 56.7°, and 62.9° are assigned as the characteristic peaks of the ZnO hexagonal wurtzite phase with a $P6_3mc$ space group (JCPDS No. 36-1451).[14,48,49] Interestingly, even if the characteristic peaks of g-$C_3N_4$ and ZnO are observed on all of the samples, their relative intensities vary from each other. First, Thio and DCDA–CNZ show sharp XRD characteristic peaks for ZnO without any disappearance and peak shift, indicating the consistency of the ZnO structures even after the formation of composites with g-$C_3N_4$. Meanwhile, in Urea–CNZ, a large and broad XRD characteristic peak for g-$C_3N_4$ is observed at 28.34°, implying the formation of a crystalline structure of g-$C_3N_4$ and its dominance on the morphological structure. The characteristic peak of g-$C_3N_4$ also appears on Thio–CNZ, but its relative intensity is very

small. Therefore, the relative crystallinity of g-$C_3N_4$ on Thio–CNZ is on the median level among the CNZ composites. Meanwhile, DCDA–CNZ has no peak for g-$C_3N_4$ at all in spite of the 27% g-$C_3N_4$ content. This difference might be attributed to the unique dispersion of g-$C_3N_4$ on the ZnO particles due to the interaction between the precursors and ZnO. Wang et al. mentioned that the XRD peaks of g-$C_3N_4$ do not appear if g-$C_3N_4$ was well dispersed on the ZnO surface.[50] Therefore, g-$C_3N_4$ on DCDA–CNZ would be uniformly formed as thin layers on the ZnO surface, whereas a dominant g-$C_3N_4$ crystalline structure would be formed on Urea–CNZ. This morphological difference due to the different interactions between the g-$C_3N_4$ precursors and ZnO during the thermal polymerization process. Additionally, the Scherrer equation was used to calculate the crystalline sizes of ZnO particles in the CNZ composites. The calculated crystallite sizes of Thio–CNZ and DCDA–CNZ are almost the same, whereas Urea–CNZ is slightly smaller. The calculated crystallite sizes are listed in **Table 3.4**.

FE-SEM and HR-TEM measurements were used to investigate the morphologies of Thio, Urea, and DCDA–CNZ. The FE-SEM images of each composite are shown in **Fig. 3.14**. All of the composites exhibit a similar structure of ZnO and g-$C_3N_4$, which is in good agreement with that reported previously.[27] **Figure 3.15** shows the HR-TEM images of Thio, Urea, and DCDA–CNZ. As presented in the figure, all composites present different interfaces between ZnO and g-$C_3N_4$ despite similar amounts of g-$C_3N_4$. Thin layers of amorphous g-$C_3N_4$ in DCDA–CNZ surround the ZnO particles, thereby forming a core–shell structure in **Figs. 3.15(g,h)**. Meanwhile, g-$C_3N_4$ and ZnO in Thio and Urea–CNZ are segregated from each other without an interface combination, implying a weak interaction of urea and thiourea with the ZnO. Furthermore, the g-$C_3N_4$ morphologies in Thio and Urea–CNZ also are different from that of DCDA–CNZ. That is, Thio and Urea–CNZ contain a porous structure of g-$C_3N_4$ (**Figs. 3.15(a,b) and (d,e)**), whereas DCDA–CNZ shows amorphous thin layers of the g-$C_3N_4$ structure.[51,52] The weak interaction between ZnO and precursors on them causes self-polymerization of the precursors in the thermal polymerization steps where thiourea and urea release gas molecules, such as $NH_3$, $H_2O$, $CO_2$, $CS_2$, and $H_2S$, resulting in a porous g-$C_3N_4$ structure. Meanwhile, DCDA has a core–shell

morphology with thin layers of g-$C_3N_4$ and does not release any gas during the thermal polymerization process.[27] Therefore, the gases released from the precursor both interrupt the interaction between the precursor and ZnO and influence the formation of a porous g-$C_3N_4$ structure, resulting in the segregated morphology of Thio and Urea–CNZ. The TEM images provide an additional evidence for the existence of each phase in the CNZ composites. **Figures 3.15(c,f,i)** show the d spacing of ZnO (0.26 nm) and d spacing of g-$C_3N_4$ (0.32 nm).

The BET surface areas ($S_{BET}$) measured using the $N_2$ adsorption–desorption isotherm technique are listed in **Table 3.4**. The $S_{BET}$ values are 33.88 $m^2/g$ (Urea–CNZ), 11.66 $m^2/g$ (Thio–CNZ), and 4.64 $m^2/g$ (DCDA–CNZ), respectively. The $S_{BET}$ value of Urea–CNZ is similar to that of g-$C_3N_4$, whereas that of DCDA–CNZ is close to that of ZnO particles in literatures.[52-54] Additionally, the higher $S_{BET}$ values of Thio and Urea–CNZ compared to that of DCDA–CNZ reflect the porous g-$C_3N_4$ structure of CNZ composites, which is consistent with the TEM results.

**Table 3.4.** Physical properties of Thio, Urea, and DCDA–CNZ.

| Sample | $S_{BET}$ ($m^2/g$)* | $K_{app}$** ($10^{-2}$/min) | Crystallite size (nm)*** | Contents (%)**** | |
|---|---|---|---|---|---|
| | | | | $C_3N_4$ | ZnO |
| Thio–CNZ | 11.67 | 0.34 | 45.62 | 71.33 | 28.67 |
| Urea–CNZ | 36.89 | 0.45 | 35.19 | 70.40 | 29.60 |
| DCDA–CNZ | 4.65 | 2.39 | 43.62 | 73.03 | 26.97 |

** The values are specific BET surface areas determined using the $N_2$ adsorption/desorption technique.*

*** Apparently, reaction rate constants ($k_{app}$) were calculated from photocatalytic reaction results.*

**** The values were calculated using the Scherrer equation.*

***** The values were calculated from TGA measurements.*

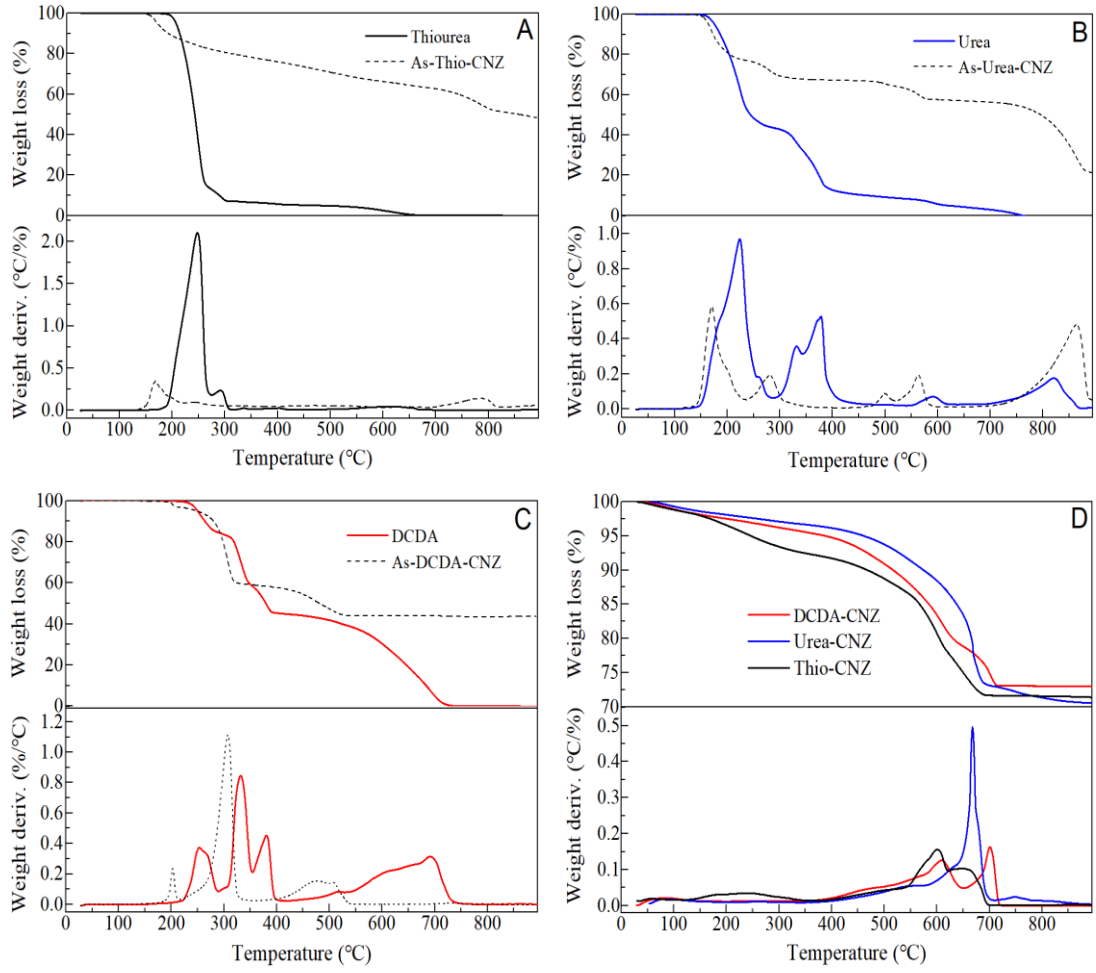


**Figure 3.12.** TGA and DTGA profiles of (A) Thiourea and As-Thio-CNZ, (B) Urea and As-Urea-CNZ, (C) Dicyandiamide and As-DCDA-CNZ, and (D) Thio, Urea, and DCDA-CNZ.

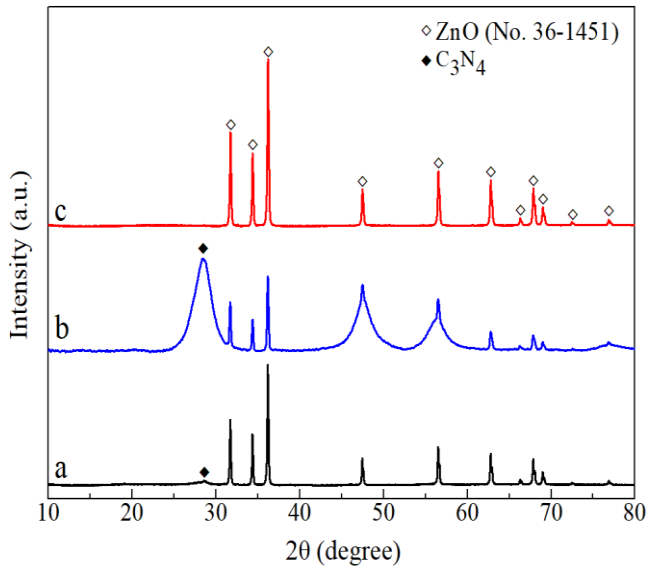


**Figure 3.13.** XRD patterns of (a-c) Thio, Urea, and DCDA-CNZ.

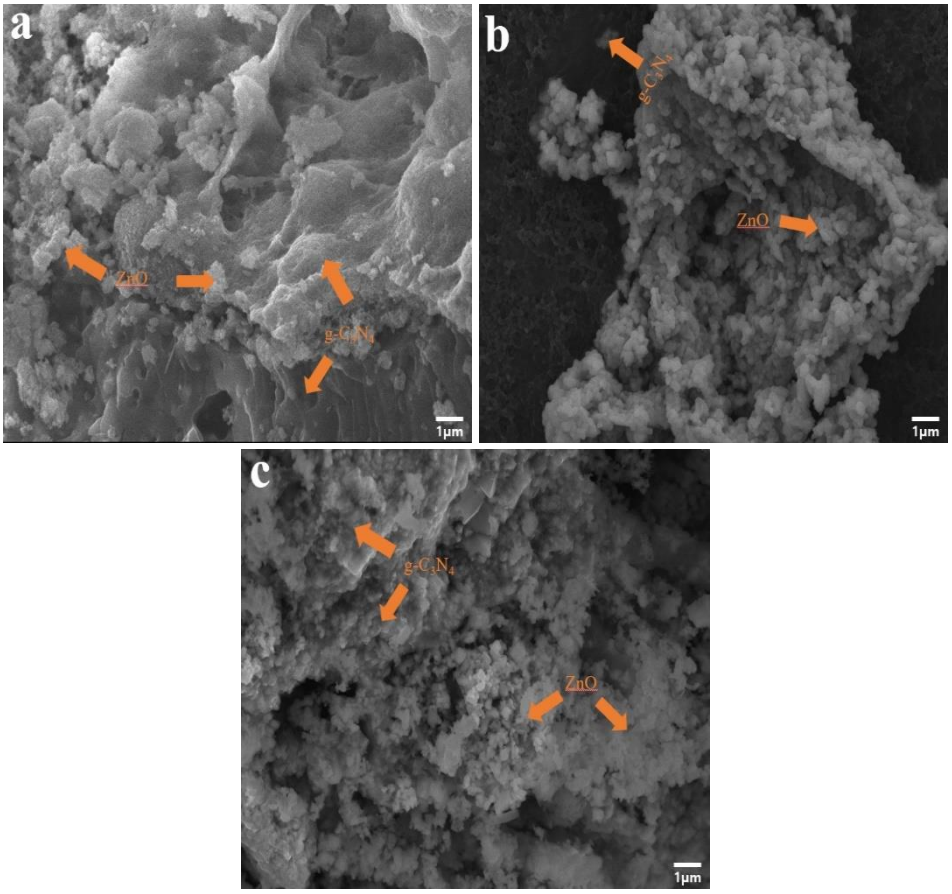


**Figure 3.14.** FE-SEM images of (a-c) Thio, Urea, and DCDA-CNZ.

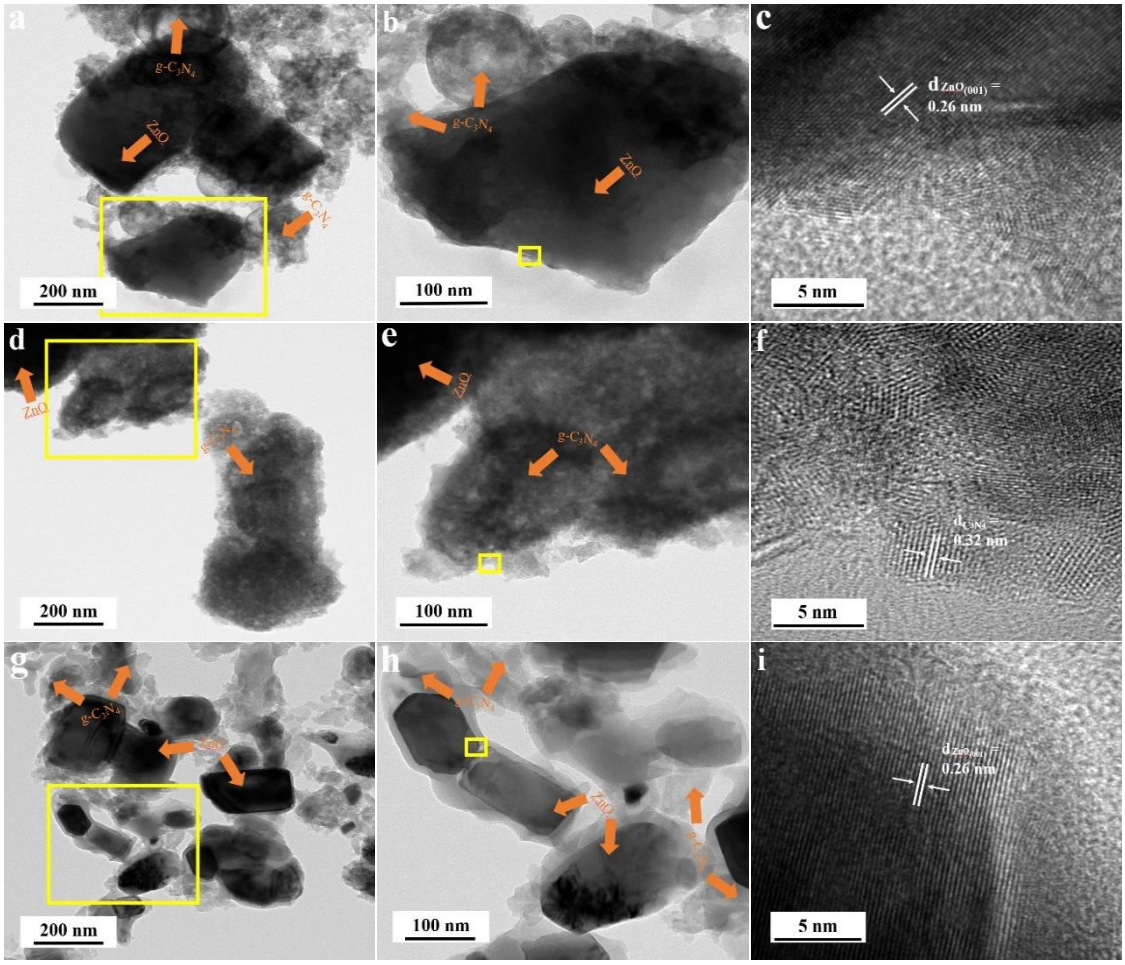


**Figure 3.15.** HR-TEM images of (a,b) Thio-CNZ, (c.d) Urea-CNZ, and (e,f) DCDA-CNZ.

### 3.2.2. Electronic and Optical Properties.

The PL and UV–vis spectra of the CNZ composites were obtained. As observed in **Fig. 3.16A**, the patterns of the PL spectra vary depending on the precursors. DCDA–CNZ exhibits a broad peak of approximately 460 nm with a shoulder at 390 nm. Meanwhile, Thio and Urea–CNZ represent a narrow and sharp peak of approximately 390 nm with a broad shoulder around 460 nm. The difference in the PL emission spectra is caused by the main band position where electrons are mainly excited on composites. In the case of Thio and Urea–CNZ, the electron excitation mainly occurs from the ZnO and then, the subsequent recombination of excited electrons emits light at 390 nm. This value approximately matches the band gap of ZnO (3.2 eV), which was reported in the previous study.[55,56] However, the emission peak of approximately 460 nm on DCDA–CNZ represents the edge emission peak of g-$C_3N_4$ and also directly corresponds to the band gap of g-$C_3N_4$ (2.67 eV), which was acquired from the fit of the UV–vis spectrum in the previous study.[41,57,58] In summary, Urea–CNZ with a segregated composite morphology mainly reflects the characteristic PL emission of ZnO, whereas DCDA–CNZ with a core–shell morphology exhibits a similar PL emission pattern of g-$C_3N_4$. Further, the lowest PL emission intensity of Urea–CNZ is caused by the low absorbance intensity of UV–Visible light. As observed in **Fig. 3.16B**, Urea–CNZ does not absorb sufficient UV–vis light to emit light in the PL spectra.

XPS analyses were employed to investigate the chemical state of elements in the CNZ composite, such as C, S, Zn, O, and S. The deconvoluted XPS data of C 1s are shown in **Fig. 3.17A**. The three deconvoluted peaks at 284.6, 287.7, and 288.8 eV are assigned to C-bonded graphitic carbon (C–C), amine groups (C–$NH_2$), and aromatic group (N–C=N).[36,38,59] The deconvoluted XPS N 1s data are also presented in **Fig. 3.17B**. The peaks at 397.6, 398.6, and 399.6 eV correspond to $sp^2$-bonded nitrogen (C–N=C), tertiary nitrogen (N–$(C)_3$), and amino functional groups in the aromatic ring (–NH), respectively. To evaluate the polymerization degree of g-$C_3N_4$ in each composite, the intensity ratio of the peak at 397.6 eV to the peak at 399.6 eV was calculated. The obtained values follow the trend of DCDA–CNZ (0.57) < Urea–

CNZ (0.89) < Thio–CNZ (1.03), implying lesser polymerized g-$C_3N_4$ in DCDA–CNZ than in Urea and Thio–CNZ. The interaction between g-$C_3N_4$ and ZnO in DCDA–CNZ interferes with the thermal formation of g-$C_3N_4$. **Figure 3.18A** shows the XPS Zn 2p data. The peaks at 1021.5 and 1044.6 eV are assigned to Zn $2p_{3/2}$ and Zn $2p_{1/2}$, respectively.[60,61] The peak position of Zn 2p on DCDA–CNZ is shifted up to 1022.1 eV by 0.6 eV, indicating the low electron density of Zn. In the literature, the strong interaction between g-$C_3N_4$ and ZnO in the core–shell morphology of DCDA–CNZ resulted in electron-deficient Zn.[41,62] Meanwhile, the peak positions of Zn 2p on Thio and Urea–CNZ are not shifted, thereby implying a weak interaction between g-$C_3N_4$ and ZnO. Moreover, the XPS data of S 2p are presented in **Fig. 3.18B**, where a sharp peak appears at 161 eV.[63] Pham and Shin also observed the S 2p peak in the XPS results of the g-$C_3N_4$/$NiTiO_3$ composite prepared using thiourea.[27] The interaction of thiourea with the $NiTiO_3$ phase resulted in a complex S 2p peak composed of several deconvoluted peaks corresponding to S linkages with various elements in $NiTiO_3$. In this study, sulfur is homogeneously deposited on Thio–CNZ and does not have any link to ZnO, which has a different behavior to g-$C_3N_4$/$NiTiO_3$ prepared using thiourea. Even if thiourea was used as the g-$C_3N_4$ precursor in both cases, the thiourea interaction with ZnO is different from that with $NiTiO_3$, resulting in different composite morphologies, that is, a segregated morphology for Thio–CNZ and an interconnected morphology for g-$C_3N_4$/$NiTiO_3$. Furthermore, gas molecules containing sulfur released from thiourea during also disturb the formation of interconnected g-$C_3N_4$ structures in Thio–CNZ.

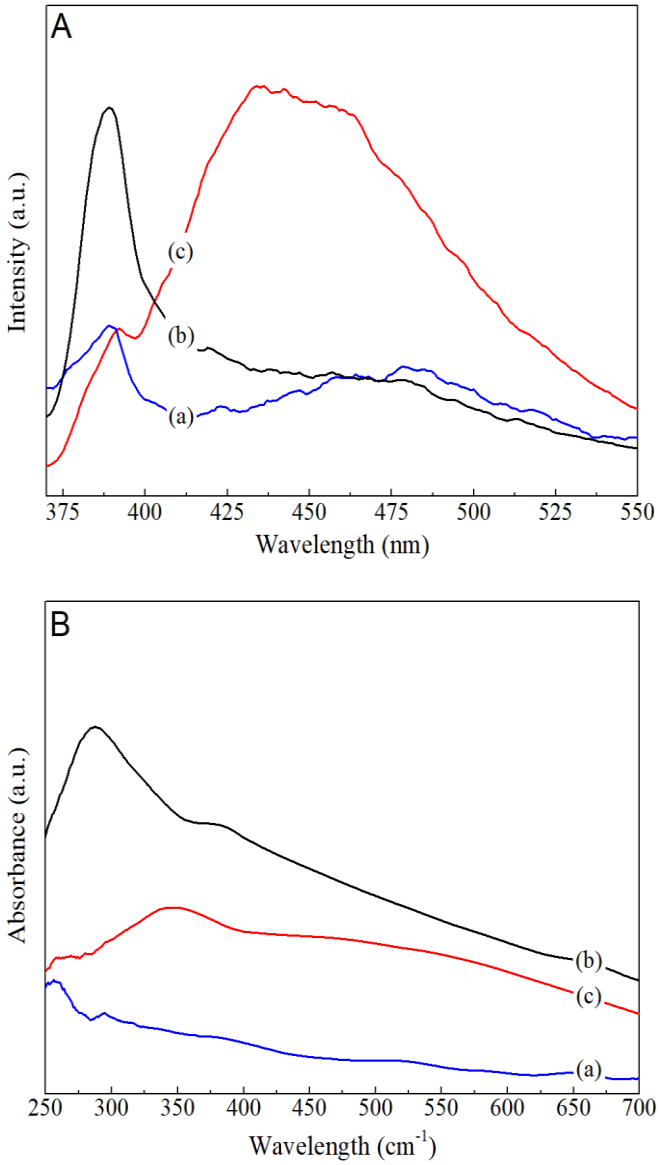


**Figure 3.16.** (A) Photoluminescence (PL) spectra and (B) UV-visible spectra of (a-c) Urea, Thio, and DCDA-CNZ.

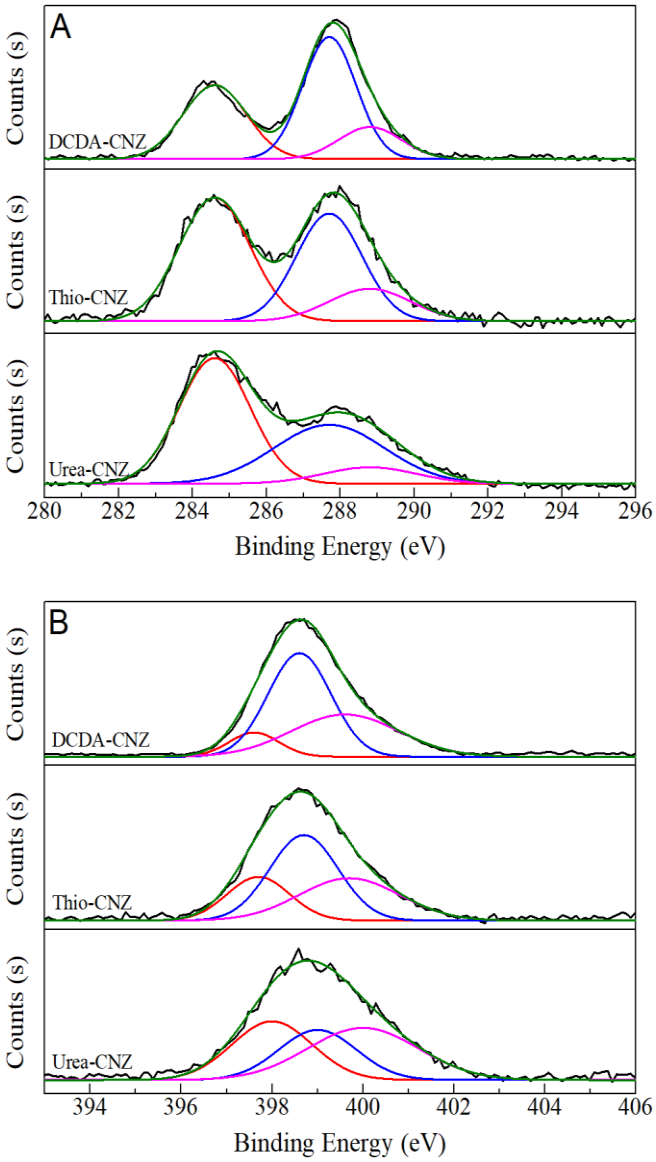


**Figure 3.17**. XPS spectra of (A) C 1s and (B) N 1s of Thio, Urea, and DCDA-CNZ.

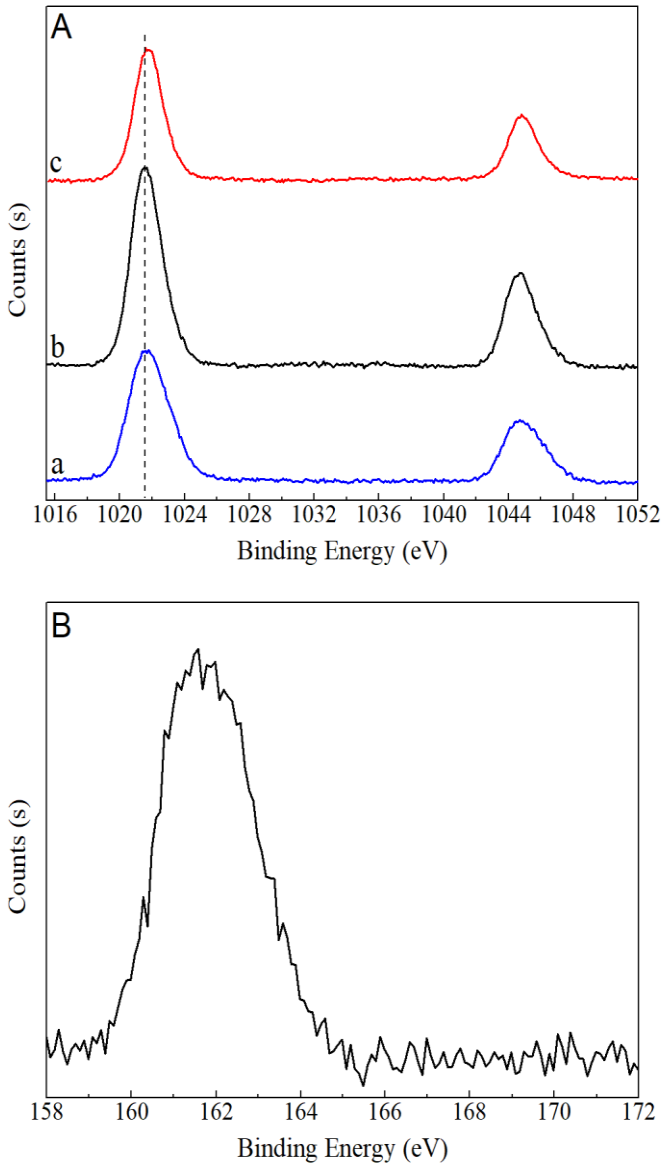


**Figure 3.18.** XPS spectra of (A) Zn 2p and (B) O 1s of Thio, Urea and DCDA-CNZ.

### 3.2.2. Photocatalysis

To simulate the photocatalytic performance of Thio, Urea, and DCDA–CNZ, photocatalytic degradation tests of MB were performed under visible-light irradiation. The MB concentrations in the solutions were plotted in **Fig. 3.19**, as well as the adsorption and photocatalytic reaction times, where DCDA–CNZ exhibits the highest MB photodegradation efficiency. The apparent reaction rate constants ($k_{app}$) were obtained by fitting the reaction data to the first-order reaction model. The obtained $k_{app}$ values are listed in **Table 3.4**. DCDA–CNZ has the highest $k_{app}$ value, indicating better photocatalytic performance than the segregated morphology of Thio and Urea–CNZ.

The best MB degradation efficiency of DCDA–CNZ is attributed to the formation of the core–shell morphology owing to the interaction between g-$C_3N_4$ and ZnO, resulting in the facilitation of the efficient charge transfer as the Z-scheme photocatalyst. As previously discussed, the PL emission spectrum of DCDA–CNZ mainly reflects the characteristic of g-$C_3N_4$, whereas Thio and Urea–CNZ show the PL emission from ZnO, indicating that the morphologies of the CNZ composites influence the optical properties. The core–shell morphology of DCDA–CNZ inhibits the recombination of electron–hole pairs using the Z-scheme charge transfer model in which the charges activated by photons are transferred from ZnO to g-$C_3N_4$.

Paradoxically, the $S_{BET}$ value of DCDA–CNZ is the lowest (i.e., 4.64 $m^2/g$), which is similar to that of ZnO. In the core–shell morphology of DCDA–CNZ, thin g-$C_3N_4$ has no effect on the $S_{BET}$ value, ZnO is dominant, as illustrated in **Fig. 3.20**. Urea–CNZ has the highest $S_{BET}$ value (36.88 $m^2/g$) because it separately contains a well-developed porous g-$C_3N_4$ structure and ZnO **(Figure 3.20)**. Therefore, in this study, DCDA is the best precursor used in preparing the CNZ composite materials because it efficiently interacts with ZnO without any gas molecules. Then, a core–shell structure with thin g-$C_3N_4$ layers is well developed on the ZnO particles. In the MB photocatalytic degradation, the core–shell morphology improves the photocatalytic activity through the Z-scheme charge transfer.

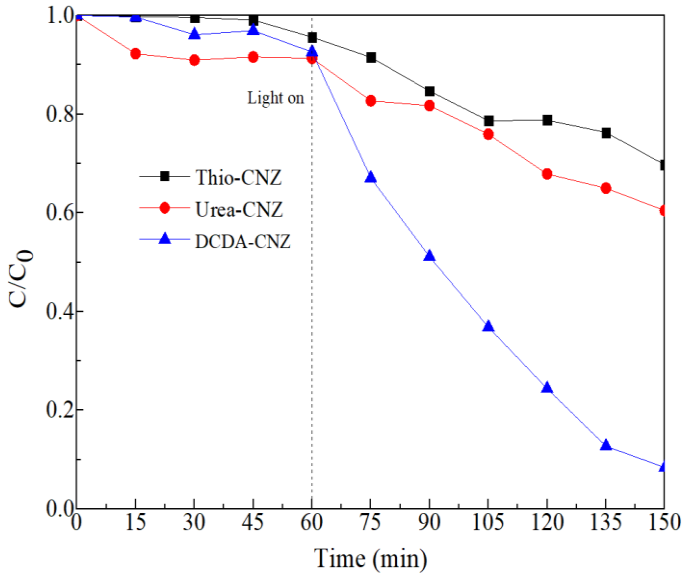


**Figure 3.19**. Photocatalytic degradation of methylene blue under visible light irradiation of Thio, Urea, and DCDA-CNZ.

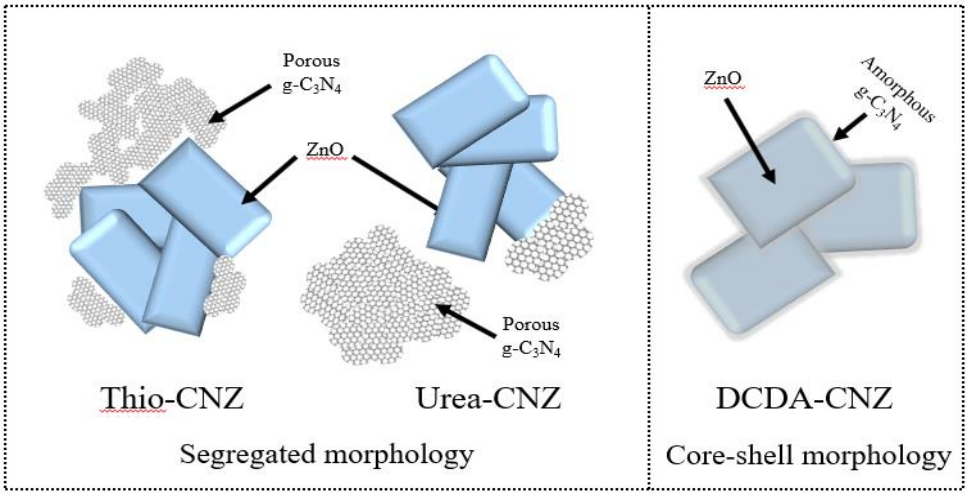


**Figure 3.20.** Schematic of the morphological structures of the CNZ composite photocatalysts.

# 4. Conclusion

In this work, we investigated the effect of annealing temperatures and precursors on interaction of ZnO and g-$C_3N_4$ in g-$C_3N_4$/ZnO composites. The reaction temperature was decreased in thermal polymerization process of precursors to the g-$C_3N_4$ in the presence of ZnO. The interaction between ZnO and g-$C_3N_4$ in the DCDA-CNZ resulted in not only thermal formation of a core-shell structure of ZnO with amorphous g-$C_3N_4$ but also a deficient electron density of Zn. The recombination of photo-generated electron-hole pairs was also inhibited in composites prepared higher annealing temperatures by the interaction in the interfaces of ZnO and g-$C_3N_4$, which follows the Z-scheme charge transfer model for composite materials. In case of Thio and Urea-CNZ, they showed a segregated morphology with porous g-$C_3N_4$ owing to the weak interaction between them and generation of gas molecules. In conclusion, the photocatalyst prepared by dicyandiamide and at 500 ℃ exhibited the highest photocatalytic activity under visible light irradiation due to the formation of Z-scheme heterojunction.

## 5. References


[1] J. Yu, J. Low, W. Xiao, P. Zhou, M. Jaroniec, Enhanced Photocatalytic $CO_2$-Reduction Activity of Anatase $TiO_2$ by Coexposed {001} and {101} Faucets, J. Am. Chem. Soc. 136 (2014) 8839-8842.

[2] Q.J. Xiang, B. Cheng, J. Yu, Graphene-Based Photocatalysts for Solar-Fuel Generation, Angew. Chem., Int. Ed. 54 (2015) 11350-11366

[3] J. Yang, D. Wang, H. Han, C. Li, Roles of Cocatalysts in Phocatalysis and Photoelectrocatalysis. Acc. Chem. Res. 46 (2013) 1900-1909

[4] J. Ran, J. Zhang, J. Yu, M. Jaroniec, S. Z. Qiao, Earth-abundant Cocatalysts for Semiconductor-based Photocatytic Water Splitting, Chem. Soc. Rev. 46 (2014) 7787-7812

[5] A. Bandyopadhyay, D. Ghosh, N.M. Kaley, S.K, Pati, Photocatalytic Activity of g-$C_3N_4$ Quantum Dots in Visible Light: Effect of Physicochemical Modifications, J. Phys. Chem. C 121 (2017) 1982-1989.

[6] H. Tada, M. Fujishima, H. Kobayashi, Photodeposition of Metal Sulfide Quantum Dots on Titanium (IV) Dioxide and the Applications to Solar Energy Conversion, Chem. Soc. Rev. 40 (2011) 4232-4243.

[7] A. L. Linsebigler, G. Lu, J. T. Yates, Jr., Photocatalysis on $TiO_2$ Surfaces: Principles, Mechanisms, and Selected Results, Chem. Rev. 95 (1995) 735-758.

[8] Y. Wang, K. Maeda, A. Thomas, K. Takanabe, G. Xin, J. M. Carlsson, K. Domen, M. Antonietti, A Metal-free Polymeric Photocatalyst for Hydrogen Production from Water under Visible Light, Nat. Mater. 8 (2009) 76-80.

[9] J. Li, M. Zhang, X. Li, Q. Li, J. Yang, Effect of the Calcination Temperature on the Visible Light Photocatalytic Activity of Direct Contact Z-scheme g-$C_3N_4$-$TiO_2$ Heterojunction, Appl. Catal. B: Environ. 212 (2017) 106-114.

[10] S. Kumar, T. Surendar, B. Kumar, A. Baruah, V. Shanker, Synthesis of Magnetically Separable and Recyclable g-$C_3N_4$-$Fe_2O_3$ Hybrid Nanocomposites with Enhanced Photocatalytic Performance under Visible-Light Irradiation, J. Phys. Chem. C 117 (2013) 261235-26143.

[11] W. J. Ong, L. L. Tan, Y. H. Ng, S. T. Yong, S. P. Chai, Graphitic Carbon Nitride (g-$C_3N_4$)-Based Photocatalysts for Artificial Photosynthesis and Environmental Remediation: Are We a Step Closer To Achieving Sustainability?, Chem. Rev. 116 (2016) 7159-7329.

[12] J. Low, C. Jiang, B. Cheng, S. Wageh, A. A. Al-Ghamdi, J. Yu, A Review of Direct Z-scheme Photocatalysts, Small Methods 1 (2017) 1700080 1-21.

[13] Z. Huang, Q. Sun, K. Lv, Z. Zhang, M. Li, B. Li, Effect of Contact Interface between $TiO_2$ and g-$C_3N_4$ on the Photoreactivity of g-$C_3N_4$/$TiO_2$ Photocatalyst: (0 0 1) vs (1 0 1) Facets of $TiO_2$, Appl. Catal. B: Environ. 164 (2015) 420-427.

[14] A. Umar, R. Kumar, G. Kumar, H. Algarni, S. H. Kim, Effect of Annealing Temperature on the Properties and Photocatalytic Efficiencies of ZnO Nanoparticles, J. Alloy Comp. 648 (2015) 46-52.

[15] C. Tian, Q. Zhang, A. Wu, M. Jiang, Z. Liang, B. Jiang, H. Fu, Cost-effective Large-scale Synthesis of ZnO Photocatalyst with Excellent Performance for Dye Photodegradation, Chem. Commun. 48 (2012) 2858-2860.

[16] W. L. Yu, D. F. Xu, T. Y. Peng, Enhanced Photocatalytic Activity of g-$C_3N_4$ for Selective $CO_2$ Reduction to $CH_3OH$ via Facile Coupling of ZnO: a Direct Z-scheme Mechanism, J. Mater. Chem. A 3 (2015) 19936-19947.

[17] L. Liu, X. Luo, F. Xu, Z. Gao, X. Zhang, Y. Song, H. Xu, H. Li, Facile Synthesis of Few-layer g-$C_3N_4$/ZnO Composite Photocatalyst for Enhancing Visible Light Photocatalytic Performance of Pollutant Removal, Colloids and Surf. A 537 (2018) 516-523.

[18] J. Wang, X. Yi, H. Zhao, G. Wang, L. Xiang, J. Xu, S. Komarneni, Oxygen Defects-Mediated Z-scheme Charge Separation in g-$C_3N_4$/ZnO Photocatalysts for Enhanced Visible-light Degradation of 4-chloropheno and Hydrogen Evolution, Appl. Catal. B: Environ. 206 (2017) 406-416.

[19] Z. Xing, Y. Chen, C. Liu, J. Yang, Y. Situ, H. Huang, Synthesis of Core-shell ZnO/oxygen Doped g-$C_3N_4$ Visible Light Driven Photocatalyst via Hydrothermal Method, J. Alloys and Comp. 708 (2017) 853-861.

[20] H. Osman, Z. Su, X. Ma, Efficient Photocatalytic Degradation of Rhodamine B Dye Using ZnO/graphitic $C_3N_4$ Nanocomposites Synthesized by Microwave, Environ, Chem. Lett. 15 (2017) 435-441.

[21] J. Wang, J. Huang, H. Xie, A. Qu, Synthesis of g-$C_3N_4$/$TiO_2$ with Enhanced Photocatalytic Activity for $H_2$ Evolution by a Simple Method, Int. J. Hydrogen Ener. 39 (2014) 6354-6363.

[22] A. Qu, X. Xu, H. Xie, Y. Zhang, J. Wang, Effects of Calcining Temperature on Photocatalysis of g-$C_3N_4$/$TiO_2$ Composites for Hydrogen Evolution from Water, Mater. Res. Bull. 80 (2016) 167-176.

[23] S. Le, T. Jiang, Y. Li, Q. Zhao, Y. Li, W. Fang, M. Gong, Highly efficient visible-light-driven mesoporous graphitic carbon nitride/ZnO nanocomposite photocatalysts, Appl. Catal. B: Environ. 200 (2017) 601-610.

[24] L. Wang, C. Ma, Z. Guo, Y. Lv, W. Chen, Z. Chang, Q. Yuan, H. Ming, J. Wang, In-situ growth of g-$C_3N_4$ layer on ZnO nanoparticles with enhanced photocatalytic performances under visible light irradiation, Mater. Lett. 188 (2017) 347-350.

[25] D. Chen, K. Wang, D. Xiang, R. Zong, W. Yao, Y. Zhu, Significantly enhancement of photocatalytic performances via core–shell structure of ZnO@mpg-$C_3N_4$, Appl. Catal. B: Environ. 147 (2014) 554-561.

[26] H. Dong, X. Guo, C. Yang, Z. Ouyang, Synthesis of g-$C_3N_4$ by different precursors under burning explosion effect and its photocatalytic degradation for tylosin, Appl. Catal. B: Environ. 230 (2018) 65-76.

[27] T.-T. Pham, E.W. Shin, Influence of g-$C_3N_4$ Precursors in g-$C_3N_4$/$NiTiO_3$ Composites on Photocatalytic Behavior and the Interconnection between g-$C_3N_4$ and $NiTiO_3$, Langmuir, 34 (2018) 13144-13154.

[28] J. Tian, Q. Liu, A. M. Asiri, K. A. Alamry, X. Sun, Ultrathin Graphitic $C_3N_4$ Nanosheets/Graphene Composites: Efficient Organic Electrocatalyst for Oxygen Evolution Reaciton, ChemSusChem, 7 (2014) 2125-2130.

[29] N. Tian, H. Huang, Y. He, Y. Guo, Y. Zhang, Organic-inorganic Hybrid Photocatalyst g-$C_3N_4$/$Ag_2CO_3$ with Highly Efficient Visible-light-active Photocatalytic Activity, Colloid. Surface. A 467 (2015) 188-194.

[30] T.-T. Pham, E. W. Shin, Thermal formation effect of g-$C_3N_4$ structure on the visible light driven photocatalysis of g-$C_3N_4$/$NiTiO_3$ composite photocatalysts, Appl. Surf. Sci. 447 (2018) 757-766.

[31] F. Fina, S. K. Callear, G. M. Carins, J. T. S. Irvine, Structural Investigaion of Graphitic Carbon Nitride via XRD and Neutron Diffraction, Chem. Mater. 27 (2015) 2612-2618.

[32] Y. Li, H. Xu, S. Ouyang, D. Lu, X. Wang, D. Wang, J. Ye, In situ Surface Alkalinized g-$C_3N_4$ toward Enhancement of Photocatalytic $H_2$ Evolution under Visible-light Irradiation, J. Mater. Chem. A 4 (2016) 2943-2950.

[33] Y. Kang, Y. Yang, L.-C. Yin, X. Kang, G. Liu, H.-M. Cheng, An Amorphous Carbon Nitride Photocatalyst with Greatly Extended Visible-Light-Responsive Range for Photocatalytic Hydrogen Generation, Advanced Materials 27 (2015) 4572-4577.

[34] H. Nguyen-Phu, C. Park, E. W. Shin, Activated Red Mud-supported Zn/Al Oxide Catalysts for Catalytic Conversion of Glycerol to Glycerol Carbonate: FTIR Analysis, Catal. Commun. 85 (2016) 52-56.

[35] H. Nguyen-Phu, C. Park, E. W. Shin, Dual Catalysis over ZnAl Mixed Oxides in the Glycerolysis of Urea: Homogeneous and Heterogeneous Reaction Routes, Appl. Catal. A:Gen. 552 (2018) 1-10.

[36] H.-J. Li, B.-W. Sun, D.-J. Qian, M. Chen, Preparation of Water-dispersible Porous g-$C_3N_4$ with Improved Photocatalytic Activity by Chemical Oxidation, Phys. Chem. Chem. Phys. 17 (2015) 3309-3315.

[37] A. Lazauskas, J. Baltrusaitis, L. Puodziukynas, M. Andrulevicius, G. Bagdziunas, D. Volyniuk, S. Meskinis, S. Niaura, T. Tamulevicius, V. Jankauskaite, Characterization of Urea Derived Polymeric Carbon Nitride and Resultant Thermally Vacuum Deposited Amorphous Thin Films: Structural, Chemical and Photophysical Properties, Carbon 107 (2016) 415-425.

[38] J.-Z. Kong, H.-F. Zhai, W. Zhang, S.-S. Wang, X.-R. Zhao, M. Li, H. Li, A.-D. Li, D. Wu, Visible Light-driven Photocatalytic Performance of N-doped ZnO/g-$C_3N_4$ Nanocomposites, Nanoscale Res. Lett. 12 (2017) 526-535.

[39] H. Tian, H. Fan, J. Ma, L. Ma, G. Dong, Noble Metal-free Modified Electrode of Exfoliated Graphitic Carbon Nitride/ZnO Nanosheets for Highly Efficient Hydrogen Peroxide Sensing, Electrochim. Acta 247 (2017) 787-794.

[40] Y. He, Y. Wang, L. Zhang, B. Teng, M. Fan, High-efficiency Conversion of $CO_2$ to Fuel over ZnO/g-$C_3N_4$ Photocatalyst, Appl. Catal. B Environ. 168 (2015) 1-8.

[41] J.-X. Sun, Y.-P. Yuan, L.-G. Qiu, X. Jiang, A.-J. Xie, Y.-H. Shen, J.-F. Zhu, Fabrication of Composite Photocatalyst g-$C_3N_4$-ZnO and Enhancement of Photocatalytic Activity under Visible Light, Dalton Transactions 41 (2012) 6756-6763.

[42] F. Guo, W. Shi, W. Guan, H. Huang, Y. Liu, Carbon Dots/g-$C_3N_4$ Nanocomposite as Efficient Visible-light Driven Photocatalyst for Tetracycline Total Degradation, Sep. purif. Technol. 173 (2017) 295-303.

[43] L. T. M. Oanh, L. T. Hang, N. D. Lai, N. T. Phuong, D. V. Thang, N. M. Hung, D. D. Bich, N. V. Minh, Influence of Annealing Temperature on Physical Properties and Photocatalytic Ability of g-$C_3N_4$ Nanosheets Synthesized through Urea Polymerization in Ar Atmosphere, Physica B 532 (2018) 48-53.

[44] Y. Yuan, L. Zhang, J. Xing, M. I. B. Utama, X. Lu, K. Du, Y. Li, X. Hu, S. Wang, A. Genc, R. Dunin-Borkowski, J. Arbiol, Q. Xiong, High-yield Synthesis and Optical Properties of g-$C_3N_4$, Nanoscale 7 (2015) 12343-12350.

[45] M. Xu, L. Han, S. Dong, Facile fabrication of highly efficient g-$C_3N_4$/$Ag_2O$ heterostructured photocatalysts with enhanced visible-light photocatalytic activity, ACS Appl. Mater. Interfaces 5 (2013) 12533-12540.

[46] Y. Hong, C. Li, G. Zhang, Y. Meng, B. Yin, Y. Zhao, W. Shi, Efficient and stable $Nb_2O_5$ modified g-$C_3N_4$ photocatalyst for removal of antibiotic pollutant, Chem. Eng. J. 299 (2016) 74-84.

[47] J. Li, M. Zhang, Q. Li, J. Yang, Enhanced visible light activity on direct contact Z-scheme g-$C_3N_4$-$TiO_2$ photocatalyst, Appl. Surf. Sci. 391 (2017) 184-193.

[48] S.P. Adhikari, H.R. Pant, H.J. Kim, C.H. Park, C.S. Kim, Deposition of ZnO flowers on the surface of g-$C_3N_4$ sheets via hydrothermal process, Ceram. Int. 41 (2015), 12923-12929.

[49] V.L. Chandraboss, J. Kamalakkannan, S. Prabha, S. Senthilvelan, An efficient removal of methyl violet from aqueous solution by an AC-Bi/ZnO nanocomposite material, RSC Adv. 5 (2015) 25857-25869.

[50] Y. Wang, R. Shi, J. Lin, Y. Zhu, Enhancement of photocurrent and photocatalytic activity of ZnO hybridized, Energy Environ. Sci. 4 (2011) 2922-2929.

[51] F. Goettmann, A. Fischer, M, Antonietti, A. Thomas, Chemical Synthesis of Mesoporous Carbon Nitrides Using Hard Templates and Their Use as a Metal-Free Catalyst for Friedel–Crafts Reaction of Benzene, Angew. Chem., Int. Ed. 45 (2006) 4467-4471.

[52] Y. Zhang, J. Liu, G. Wu, W. Chen, Porous graphitic carbon nitride synthesized via direct polymerization of urea for efficient sunlight-driven photocatalytic hydrogen production, Nanoscale 4 (2012) 5300-5303.

[53] D. J. Martin, K. Qiu, S.A. Shevlin, A.D. Handoko, X. Chen, Z. Guo, J. Tang, Highly efficient photocatalytic $H_2$ evolution from water using visible light and structure-controlled graphitic carbon nitride, Angew. Chem., Int. Ed. 53 (2014) 9240-9245.

[54] J. Xu, Y. Li, S. Peng, G. Lu, S. Li, Eosin Y-sensitized graphitic carbon nitride fabricated by heating urea for visible light photocatalytic hydrogen evolution: the effect of the pyrolysis temperature of urea, Phys. Chem. Chem. Phys. 15 (2013) 7657-7665.

[55] H. Lv, G. Ji, Z. Yang, Y. Liu, X. Zhang, W. Liu, H. Zhang, Enhancement photocatalytic activity of the graphite-like $C_3N_4$ coated hollow pencil-like ZnO, J. Colloid Interface Sci. 450 (2015) 381-387.

[56] W.K. Jo, N.C.S. Selvam, Enhanced visible light-driven photocatalytic performance of ZnO–g-$C_3N_4$ coupled with graphene oxide as a novel ternary nanocomposite, J. Hazard. Mater. 299 (2015) 462-470.

[57] S. Zhang, Y. Yang, Y. Guo, W. Guo, M. Wang, Y. Guo, Y. Huo, Preparation and enhanced visible-light photocatalytic activity of graphitic carbon nitride/bismuth niobate heterojunctions, J. Hazard. Mater. 261 (2013) 235-245.

[58] X. Wang, S. Blechert, M. Antonietti, Polymeric graphitic carbon nitride for heterogeneous photocatalysis, ACS Catal. 2 (2012) 1596-1606.

[59] R.C. Pawar, Y. Son, J. Kim, S.H. Ahn, C.S. Lee, Integration of ZnO with g-$C_3N_4$ structures in core–shell approach via sintering process for rapid detoxification of water under visible irradiation, Curr. Appl. Phys. 16 (2016) 101-108.

[60] P.-Y. Kuang, Y.-Z. Su, G.-F. Chen, Z. Luo, S.-Y. Xing, N. Li, g-$C_3N_4$ decorated ZnO nanorod arrays for enhanced photoelectrocatalytic performance, Appl. Surf. Sci. 358 (2015) 296-303.

[61] R.C. Pawar, D.-H. Choi, J.-S. Lee, C.S. Lee, Formation of polar surfaces in microstructured ZnO by doping with Cu and applications in photocatalysis using visible light, Mater. Chem. Phys. 151 (2015) 167-180.

[62] X. Yuan, S. Duan, G. Wu, L. Sun, G. Cao, D. Li, H. Xu, Q. Li, D. Xia, Enhanced catalytic ozonation performance of highly stabilized mesoporous ZnO doped g-$C_3N_4$ composite for efficient water decontamination, Appl. Catal. B:Gen. 551 (2018) 129-138.

[63] G. Zhang, J. Zhang, M. Zhang, X. Wang, Polycondensation of thiourea into carbon nitride semiconductors as visible light photocatalysts, J. Mater. Chem. 22 (2012) 8083-8091.